

Dependence of trefoil vortex knots upon the initial vorticity profile.

Robert M. Kerr

*Department of Mathematics, University of Warwick,
Coventry CV4 7AL, United Kingdom. email: Robert.Kerr@warwick.ac.uk*

Six sets of Navier-Stokes trefoil vortex knots in $(2\pi)^3$ domains show how the shape of the initial profile influences the evolution of the enstrophy Z , helicity \mathcal{H} and dissipation-scale. Significant differences develop even when all have the same three-fold symmetric trajectory, the same initial circulation and the same range of the viscosities ν . Maps of the helicity density $h = \mathbf{u} \cdot \boldsymbol{\omega}$ onto vorticity isosurfaces patches show where $h \lesssim 0$ sheets form during reconnection. For the Gaussian/Lamb-Oseen profile helicity \mathcal{H} grows significantly, with only a brief spurt of enstrophy growth as thin braids form then decay during reconnection. The remaining profiles are algebraic. For the untruncated algebraic cases, $h < 0$ vortex sheets form in tandem with ν -independent convergence of $\sqrt{\nu}Z(t)$ at a common t_x . For those with the broadest wings, enstrophy growth accelerates during reconnection, leading to approximately ν -independent convergent finite-time dissipation rates $\epsilon = \nu Z$. By mapping terms from the budget equations onto centerlines, the origins of the divergent behavior are illustrated. Lamb-Oseen has six locations of centerline convergence form with local negative helicity dissipation, $\epsilon_h < 0$, and small, but positive h . Later, the sum of these localized patches of $\epsilon_h < 0$ leads to a positive increase in the global \mathcal{H} and suppression of enstrophy production. For the algebraic profiles: There are only three locations of centerline convergence, each with spans of less localized $\epsilon_h < 0$ and some $h < 0$. Spans that could be the seeds for the $h < 0$ vortex sheets that form in the lower half of the trefoil as the $\sqrt{\nu}Z(t)$ phase begins and can explain accelerated growth of the enstrophy and evidence for finite-time energy dissipation ΔE_ϵ . Despite the initial symmetries.

I. BACKGROUND

For the incompressible, three-dimensions Navier-Stokes equation the three significant quadratic integrated diagnostics of the velocity \mathbf{u} and vorticity $\boldsymbol{\omega}$ are: the kinetic energy with $E \sim 0.5u^2$; the enstrophy with $Z \sim \omega^2$; and the helicity \mathcal{H} . \mathcal{H} is the global integral of the helicity density $h = \mathbf{u} \cdot \boldsymbol{\omega}$ and can take either sign. Equations representing their budgets are defined in section II.

The robust relationship between the energy E and enstrophy Z is well-known. Given a viscosity ν , the energy dissipation rate $dE/dt = \epsilon$ with $\epsilon = \nu Z$. The importance of ϵ for turbulent flows is that irregularity of the vorticity can lead to very large enstrophy and a energy dissipation rate ϵ that is large enough to support a finite, Reynolds number-independent energy dissipation. This is known as a *dissipation anomaly*, defined as the finite integral

$$\Delta E_\epsilon = \int_0^{T_\epsilon} \epsilon dt > 0 \quad \text{in a finite-time } T_\epsilon. \quad (1)$$

This is observed in many laboratory and environmental turbulent flows. This relation between irregular vorticity and turbulent decay is robust, but has this caveat: Can a smooth initial state far from boundaries numerically generate $\nu \rightarrow 0$ finite ΔE_ϵ without either forcing or a parameterized dissipation ϵ ?

Could a better understanding of the helicity density h help? What is known is that without viscosity, that is for the inviscid $\nu = 0$ Euler equations, the global helicity \mathcal{H} is preserved, in addition to the energy E . And on that basis it has been proposed that \mathcal{H} can constrain nonlinear Euler growth of the enstrophy Z . However, could the formation of local $h < 0$ along a vortex lead to a alternative scenario?

Trefoil vortex knots are an initial state that is inherently helical, self-reconnecting, and mathematically compact, meaning that they can be isolated far from boundaries. The goal of this paper is to revisit recent trefoil knots simulations [1–4] to ascertain why different initial vorticity profiles generate starkly contrasting answers to those questions.

Before the results in papers [1–4], the most that numerics has been able to tell us about the role of helicity is that for single-signed helical Fourier modes, energy dissipation can be suppressed for a short time [5]. These flows then evolve into traditional decaying numerical turbulence: without any further insight into whether h has a role in either achieving, or suppressing, finite energy dissipation as the viscosity decreases.

Could trefoil vortex knots robustly overcome those limitations? Robustly meaning, are the numerics adequate to reach consistent conclusions? One conclusion coming from comparing the recent trefoil papers is that the results are not robust. With different initial states or numerics, different trends are observed for the evolution of the enstrophy $Z(t)$ and helicity $\mathcal{H}(t)$, particularly as reconnection begins and immediately afterward.

To illustrate the differences, figures 1 and 2 compare $Z(t)$ and $\mathcal{H}(t)$ for two sets of calculations with the same circulation $\Gamma = 1$ (7) and same three-fold symmetric trajectories, but representing different initial core profiles. Respectively, evolution using a Gaussian/Lamb-Oseen (10) core profile, as recently reported [3], and from a $p_r = 1$

algebraic core (9) that has already provided evidence for a dissipation anomaly, finite ΔE_ϵ (1) [2]. Another difference in their initialization is the vortex core width.

How do $Z(t)$ and $\mathcal{H}(t)$ evolve for these cases? At very early times and for all the profiles, $Z(t)$ decreases, meaning more enstrophy dissipation than production. This similarity between the two continues only until $t = 0.4$. After which $Z(t)$ and $\mathcal{H}(t)$ diverge slowly until the innermost (centerline) vorticity isosurfaces begin to reconnect at a common time of $t_r \approx 4$. Then as $t \rightarrow t_r$, the differences become dramatic. For Lamb-Oseen, after some enstrophy growth at $t \sim t_r$, its enstrophy $Z(t)$ decreases again while the helicity \mathcal{H} grows. With thin vortex bridges and braids forming, as previously observed [3] and discussed in section III C.

In contrast, for the three-fold symmetric trefoils with a $p_r = 1$ algebraic profile, while reconnection begins at the same t_r , it is not completed until a somewhat later time of t_x . Figure 3a defines t_x as when there is ν -independent convergence of $\sqrt{\nu}Z(t)$, a ‘reconnection-enstrophy’. Convergence that has previously been associated with the formation of vortex sheets [2]. Figure 16 in section III B goes further: showing that the vortex sheets have $h < 0$.

However convergence of $\sqrt{\nu}Z(t)$ is not convergence of the dissipation rates $\epsilon(t) = \nu Z(t)$. What has been found for algebraic trefoils with perturbations, in far larger domains, is that convergence of $\epsilon(t) = \nu Z(t)$ in a finite time is possible [2]. Can the algebraic calculations reported here develop finite-time convergence of $\epsilon(t) = \nu Z(t)$: despite the three-fold symmetry and a tighter domain?

They do, with figure 3b providing evidence for weak convergence of the dissipation rates $\epsilon(t) = \nu Z(t)$ at $t_\epsilon \approx 2t_x$. In figure 2 this is accompanied by a modest increase in $\mathcal{H}(t)$ at the higher Reynolds numbers before \mathcal{H} decays. This is discussed in section III D.

To complete the discussion of profiles, a set calculations using the $p_r = 2$ Rosenhead regularized profile (9) of a point vorticity [6] is discussed in section III E. The mathematics community calls this the Kaufman-Sculley profile and it will be designated as the K-S-R profile here. The shape of the central core is intermediate between the two others, but its overall behavior is closer to that of the $p_r = 1$ algebraic profile.

Given these differences in the $Z(t)$ and $\mathcal{H}(t)$ evolution, these questions can be asked (tentative answers in parentheses).

- Can the $t \sim 0$ origins of the divergent behavior be identified? (The Rayleigh inflection-point instability discussed in section II B.)
- What are the differences in the post-reconnection $t > t_x$ dissipative structures? (Sheets lead to a *dissipation anomaly*, braids and bridges do not.)
- Are there diagnostics for identifying the intervening, divergent $0 < t < t_r$ dynamics? (Mapping terms in the enstrophy and helicity budgets onto vortices’ centerlines.)

To reduce the number of possible sources for those differences, all of the new calculations are three-fold symmetric and run in $(2\pi)^3$ periodic domains. This ensures that the only differences between each set of trefoils are the choices of their initial vorticity profiles and their widths.

Figure 4 provides an early time, three-dimensional perspective on the vorticity isosurfaces at $t = 1.2$ for algebraic case r1d015 and Lamb-Oseen Gd05. In terms of the overall structure they are almost identical. Perhaps the only identifiable difference is the different positions of the maximum of vorticity $\omega_m = \|\omega\|_\infty$, indicated by **X**. For the algebraic case on the left, ω_m is co-located with the blue triangle, maximum of helicity h_{mx} . For Lamb-Oseen on the right, ω_m is at the maroon diamond, a local minima of the helicity flux (6), $\min(h_f)$. However, on the centerlines their respective enstrophy and helicity density budgets are quite different.

The paper is organized as follows. After the introduction of the profile-dependent evolution of the primary global diagnostics, and their early vorticity isosurfaces, the governing and budget equations are given. Next are the steps required to initialize the vortices, including how the raw, unbalanced mapped vorticity fields are made incompressible. Once the initial profiles are defined, recent mathematics for determining their stability is referenced and a new set of diagnostics are defined that map the terms from the enstrophy and helicity budget equations (5,6) onto the evolving centerline trajectories. Up to $t = 3.6$, both helicity-mapped vorticity isosurfaces and mapped centerline budgets are used in the comparisons between the evolution of cases Gd05 (Gaussian/Lamb-Oseen) and r1d015 ($p_r = 1$, $r_o = 0.015$ algebraic). The $t < t_r = 4$ differences in the budget terms lead to profound differences in the $t \gtrsim 4$ dissipative structures and dissipation rates $\epsilon(t)$. For Lamb-Oseen at and after reconnection: thin bridges, then braids and decaying dissipation rates. While for all of the algebraic calculations: vortex sheets start to form with $\sqrt{\nu}Z(t)$ convergence for $t_x \lesssim 1.5t_r$; and for the widest initial algebraic profiles, ν -independent dissipation rates ϵ that approximately converge at $t_\epsilon \approx 2.5t_r$.

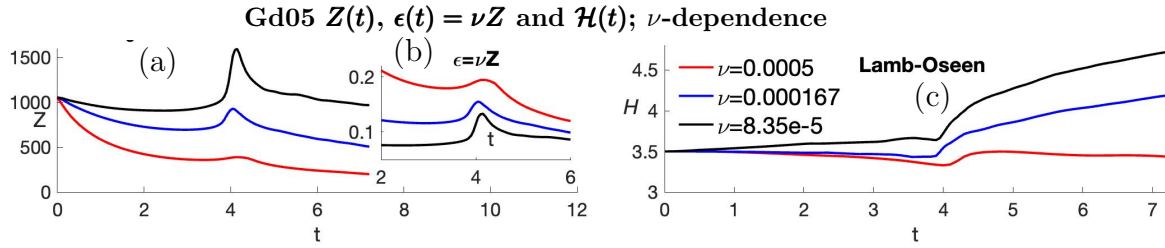


FIG. 1: Time dependence of (a) the enstrophy $Z(t)$, dissipation rate $\epsilon(t) = \nu Z$ (inset) and (c) global helicity $\mathcal{H}(t)$ for case Gd05, a three-fold symmetric trefoil with a Gaussian/Lamb-Oseen profile (10). Three viscosities (in legend) are given, whose Reynolds numbers are [2000 6000 12000]. Similar to figure 3 of [3]. All calculations are in $(2\pi)^3$ periodic boxes.

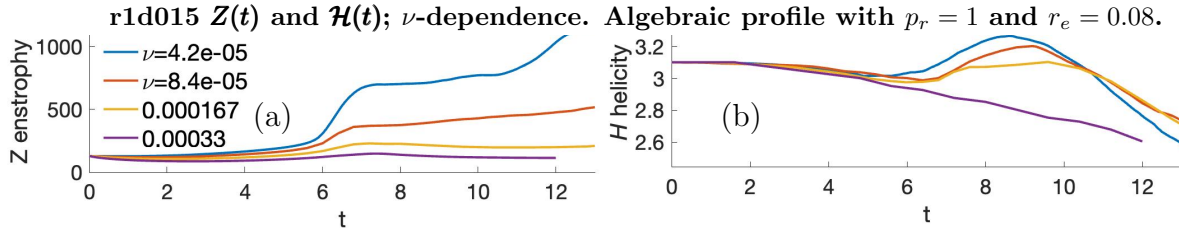


FIG. 2: Time dependence of (a) the enstrophy $Z(t)$ and (b) the global helicity $\mathcal{H}(t)$ for algebraic (9) case r1d015, with $p_r = 1$, $r_o = 0.015$ and $r_e = 0.08$, at several viscosities (in legend) with Reynolds numbers [24000 12000 6000 3000].

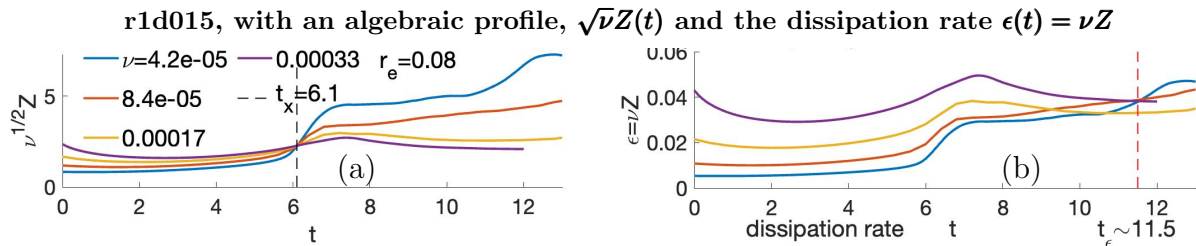


FIG. 3: For the case and viscosities in figure 2: (a) time dependence of the reconnection-entrophy $\sqrt{\nu}Z(t)$, with convergence at $t_x = 6$ that is used to define the end of the first reconnection; (b) the dissipation rate $\epsilon(t) = \nu Z$, whose convergence at $t \approx 10$ is used to define the dissipation anomaly ΔE_ϵ (1).

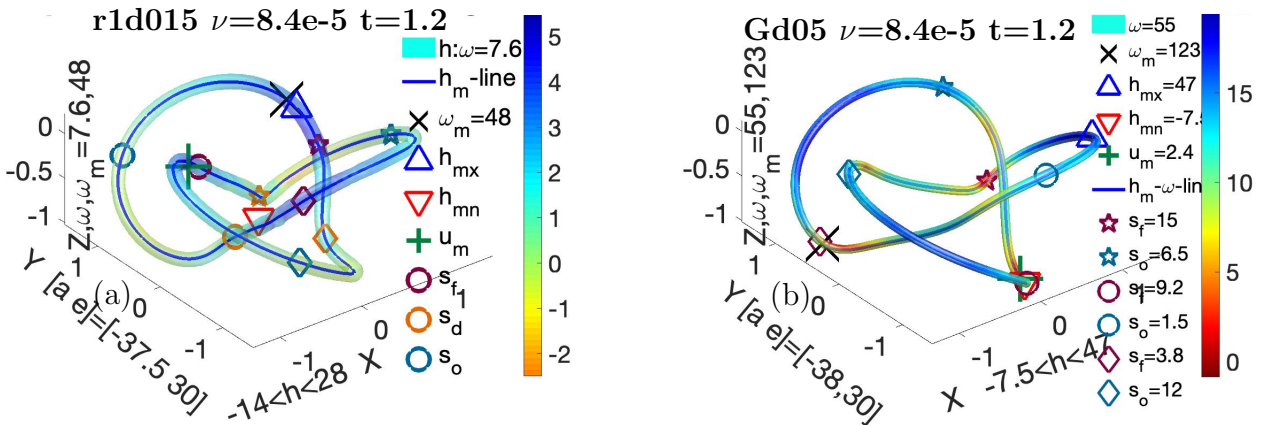


FIG. 4: Three-dimensional vorticity isosurfaces with mapped helicity at $t = 1.2$ for two of the three-fold symmetric trefoils. (a) From the $p_r = 1$, $r_o = 0.015$ algebraic (9) calculation (r1d015). (b) Lamb-Oseen profile (10) (Gd05). The primary extrema of interest: Maximum vorticity, minima and maxima of the helicity, and the maximum velocity are indicated in both frames, with symbols in the legends. In addition, each frame indicates the three-dimensional positions of the s_f , local min(h_f), and their opposing s_o points, closest points in 3D on their opposite loops. For the algebraic, the s_d , local min(ϵ_h). These are also marked on the $t = 1.2$ centerline budget profiles in figures 9 and 11 and will be used for reference at later times.

II. EQUATIONS, NUMERICS, INITIAL CONDITIONS, CENTERLINE MAPS, STABILITY.

The governing equations are the incompressible Navier-Stokes equations: for the velocity

$$\frac{\partial \mathbf{u}}{\partial t} + (\mathbf{u} \cdot \nabla) \mathbf{u} = -\nabla p + \underbrace{\nu \Delta \mathbf{u}}_{\text{viscous drag}}, \quad \nabla \cdot \mathbf{u} = 0; \quad (2)$$

and the vorticity $\boldsymbol{\omega} = \nabla \times \mathbf{u}$

$$\frac{\partial \boldsymbol{\omega}}{\partial t} + (\mathbf{u} \cdot \nabla) \boldsymbol{\omega} = (\boldsymbol{\omega} \cdot \nabla) \mathbf{u} + \nu \Delta \boldsymbol{\omega}, \quad \nabla \cdot \boldsymbol{\omega} = 0. \quad (3)$$

Numerics. All of the calculations are done in $(2\pi)^3$ periodic boxes with a 2/3rds-dealiased pseudo-spectral code and a high-wavenumber cutoff filter [7, 8]. These features remove aliasing errors and absorb high-wavenumber fluctuations that would otherwise be reflected (in Fourier space) from the abrupt high-wavenumber cut-off. Extensive tests showed that with these features the calculations do at least as well as a calculation on a mesh that is 1.5 times greater. Some tests, such as doubling the mesh and comparing the maximum vorticities, have been repeated here.

Based on this past experience, the evolution of the global helicity and enstrophy shown for all cases can be trusted. For the more detailed analysis on vortex lines and three-dimensional graphics, the algebraic r1d015 $\nu = 1.6\text{e-}4$ statistics are reliable for all times, but those with $\nu = 8.4\text{e-}5$ are given only to $t = 3.6$. The detailed results for case G1e3d05 $\nu = 8.4\text{e-}4$ can be trusted up to $t = 4.4$, but not for $t \geq 4.8$.

Five initial profiles are discussed, each run for at least three viscosities. A larger number of profiles were done before choosing these five, so in the interest of economy and ease of use, the vorticity graphics for cases other than Gd015 and r1d015 use 512^3 meshes. Several of the smallest viscosity calculations, and all of the Lamb-Oseen calculations, are from 1024^3 mesh calculations.

The continuum equations for the densities of the energy, enstrophy and helicity, $e = \frac{1}{2}|\mathbf{u}|^2$, $\zeta = |\boldsymbol{\omega}|^2$ and $h = \mathbf{u} \cdot \boldsymbol{\omega}$, with their production, flux and dissipation rates are:

$$\frac{\partial e}{\partial t} + (\mathbf{u} \cdot \nabla) e = -\nabla \cdot (\mathbf{u} p) + \nu \Delta e - \underbrace{\nu (\nabla \mathbf{u})^2}_{\epsilon = \text{dissipation} = \nu Z}, \quad E = \frac{1}{2} \int \mathbf{u}^2 dV; \quad (4)$$

$$\frac{\partial \zeta}{\partial t} + (\mathbf{u} \cdot \nabla) |\boldsymbol{\omega}|^2 = \underbrace{2\boldsymbol{\omega} \mathcal{S} \boldsymbol{\omega}}_{\zeta_p = \text{production}} + \nu \Delta |\boldsymbol{\omega}|^2 - \underbrace{2\nu (\nabla \boldsymbol{\omega})^2}_{\epsilon_\omega = Z - \text{dissipation}}, \quad Z = \int \boldsymbol{\omega}^2 dV; \quad (5)$$

$$\frac{\partial h}{\partial t} + (\mathbf{u} \cdot \nabla) h = \underbrace{-\boldsymbol{\omega} \cdot \nabla \Pi}_{h_f = \omega - \text{transport}} + \underbrace{\nu \Delta h}_{\nu - \text{transport}} - \underbrace{2\nu \text{tr}(\nabla \boldsymbol{\omega} \cdot \nabla \mathbf{u}^T)}_{\epsilon_h = \mathcal{H} - \text{dissipation}}, \quad \mathcal{H} = \int \mathbf{u} \cdot \boldsymbol{\omega} dV. \quad (6)$$

$\Pi = p - \frac{1}{2}\mathbf{u}^2 \neq p_h$ is not the pressure head $p_h = p + \frac{1}{2}\mathbf{u}^2$.

While the global energy E and helicity \mathcal{H} are inviscid invariants [11], their inviscid Lagrangian local densities e and h can change due to the pressure gradient $-\nabla p$ and the ω -transport h_f respectively. Under $\nu \neq 0$ Navier-Stokes, both the helicity flux h_f and dissipation ϵ_h can generate local negative helicity $h < 0$. Note that h is not locally Galilean invariant due to h_f .

Role for $h < 0$? Can local $h < 0$ break helicity's constraint upon the nonlinear growth of the enstrophy Z ? Section IID shows how this question can be addressed by mapping the budget terms onto the vorticity centerlines.

For short times another set of inviscid short-time conservation laws are the circulations Γ_i for closed loops \mathcal{C}_i about those trajectories:

$$\Gamma_i = \oint_{\mathcal{C}_i} \mathbf{u}_i \cdot \mathbf{r}_i \quad \text{where} \quad \mathbf{r}_i \text{ is a closed loop about } \mathcal{C}_i. \quad (7)$$

With the appropriate choice of the closed loop, Γ_i can be preserved during Navier-Stokes reconnection for very short times. Could this constraint that have additional consequences?

A. Initial conditions

Four elements are used to define an incompressible vortex knot.

- 1) The $\mathbf{x}(\phi)$ trajectory of the centerline of the vortex knot (8).
- 2) The vorticity profile $|\omega(\rho)|$, with the distance ρ defined as the distance between a given mesh point \mathbf{x} and the nearest point on the trajectory $\mathbf{x}(\phi)$: $\rho = |\mathbf{x} - \mathbf{x}(\phi)|$.
 - a) The profiles are either algebraic (9), with a chosen power-law p_r , or Gaussian/Lamb-Oseen (10).
 - b) Each $|\omega(\rho)|$ has two parameters: A radius r_o and the centerline vorticity ω_o .
 - The final ω_o are chosen so that the circulation $\Gamma \equiv 1$ (7) after step 4.
 - In this paper $\Gamma = 1$ and $r_f = 1$ are fixed so the nonlinear timescale for all the calculations is $t_{NL} = 1$ (8).
- 3) The chosen profile is mapped onto a Cartesian mesh using previous algorithms [1], with the direction of vorticity given by the centerline direction: $\hat{\omega}(\rho) = \hat{\omega}(\mathbf{x}(\phi))$.
- 4) Finally, we need to remove the non-solenoidal components of the raw vorticity field by projection. This also makes the velocity field incompressible. Except for the Lamb-Oseen profile, this operation invariably leads to reductions in the values of the maximum vorticity ω_m and the enstrophy Z .

The initial trajectory $\boldsymbol{\xi}_0(\phi) = [x(\phi), y(\phi), z(\phi)]$ of all the trefoils in this paper is defined over $\phi = 1 : 4\pi$ by this closed double loop, with $r_f = 1$ and $r_1 = 0$:

$$\begin{aligned}
 x(\phi) &= r(\phi) \cos(\alpha) \\
 y(\phi) &= r(\phi) \sin(\alpha) & z(\phi) &= a \cos(\alpha) \\
 \text{where } r(\phi) &= r_f + r_1 a \cos(\phi) + a \sin(w\phi + \phi_0) \\
 \text{and } \alpha &= \phi + a \cos(w\phi + \phi_0) / (wr_f) \\
 \text{with } t_{NL} &= r_f^2 / \Gamma \text{ the nonlinear time-scale,} \\
 \text{and } r_e &= (\Gamma / (\pi\omega_m))^{1/2} \text{ the effective radius.}
 \end{aligned} \tag{8}$$

The four algebraic Rosenhead regularized profiles $\omega_{\text{raw}}(\rho)$ are parameterized by a radius r_o , maximum/centerline vorticity ω_o and a power law p_r .

$$\omega_{\text{raw}}(\rho) = \omega_o \frac{(r_o^2)^{p_r}}{(\rho^2 + r_o^2)^{p_r}}. \tag{9}$$

For a columnar vortex, (14) suggests that the $p_r = 2$ K-S-R profile is stable unless there are perturbations with high azimuthal wavenumber m (13). The ‘broader’ $p_r = 1$ algebraic profile has been used as the second initialization step of several earlier papers [1, 2, 12].

The Gaussian/Lamb-Oseen profile is

$$\omega_{\text{raw}}(\rho) = \omega_o \exp(-(\rho/r_o)^2) \quad \text{for } \rho < \rho_+. \tag{10}$$

This definition of the Lamb-Oseen profile has these advantages: $\omega_m = \omega_o$ and the effective radius $r_e = r_o$, without the factor of 2 required by the Lamb-Oseen profile in current use [3]. The only difference between that profile and (10) is that the core in figure 5 is $\sqrt{2}$ wider. This, along with a different definition of the enstrophy Z (5) (a factor of 2), yields enstrophy and helicity evolution that are (in appearance) nearly identical to theirs [3].

Table I gives the details of the 5 initial profiles: The parameters, r_o and ω_o for the profile formulae (9,10), the generated raw enstrophies Z_o . Then the divergence-free $t = 0$ values: the effective radii r_e (8), vorticity maxima ω_m and enstrophies $Z(0)$. The viscosities are given in the figure legends.

An additional, inherent parameter is the maximum radius ρ_+ used to map $\omega_{\text{raw}}(\rho)$ onto the Cartesian mesh in step 3. Empirically, the trefoils’ evolution is independent of ρ_+ so long as the circulation $\Gamma = 1$ and $\rho_+ \sim 0.5 - 1$ (trefoil radius is $r_f = 1$), with $\rho_+ \geq 0.75$ for all cases here except one in the appendix. Case r1d015dm025 with $\rho_+ = 0.025$ and evolution that is similar to Lamb-Oseen.

Initial profiles. The specific profiles listed are: Lamb-Oseen (case Gd05), two broad algebraic $p_r = 1$ cases (r1d015, r1d006) and two K-S-R $p_r = 2$ cases (r2d05, r2d1). With most of the analysis figures are taken from the highest Reynolds number calculations of the Lamb-Oseen (Gd05) and the $p_r = 1$, $r_o = 0.015$ ‘broad’ algebraic profile (r1d015). Figure 4 compares their slightly evolved $t = 1.2$ three-dimensional helicity-mapped vorticity isosurfaces.

Cases	p_r	n^3	r_o	ω_o	Z_o	r_e	ω_m	$Z(0)$	ν 's	t-3D- ω
Gd05	—	1024^3	0.05	130	1057	0.05	130	1055	5e-4 1.7e-4 8.4e-5	$t \leq 4.4$
r2d05	2	512^3	0.05	64.3	326	0.07	62	306	3.3e-4 1.7e-4 8.4e-5	$t \leq 5.2$
r2d1	2	512^3	0.1	17.85	97.1	0.14	17.3	96.5	3.3e-4 1.7e-4 8.4e-5	all times
r1d006	1	1024^3	0.006	554	333	0.053	138	229	1.7e-4 8.4e-5	only Z, \mathcal{H}
r1d015	1	1024^3	0.015	100	138	0.078	56	124	1.7e-4	$t \leq 6$
r1d015	1	512^3	0.015	100	138	0.078	56	124	3.3e-4 4.2e-5	only Z, \mathcal{H}
r1d015	1	1024^3	0.015	100	138	0.078	56	124	8.4e-5	$t \leq 3.6$
r1d015dm025	1	512^3	0.015	182	362	0.056	102	325	8.4e-5	$t \leq 10$

TABLE I: Raw core radius r_o and vorticity ω_o parameters, resulting enstrophy Z_o , then effective radii $r_e(8)$, maximum vorticity ω_m and enstrophy Z after fields are made divergent-free. The t-3D- ω column is the last time for which detailed three-dimensional graphics were made for those cases. The global enstrophy $Z(t)$ and helicity $\mathcal{H}(t)$ are reliable for all cases listed. The only Lamb-Oseen case is labeled Gd05 and the algebraic cases are labeled by the power-law p_r as in r1d015: ($r1 \equiv p_r=1$) and raw core radii ($d015=r_o=0.015$). Last is r1d015dm025: ($r1 \equiv p_r=1$) with radii ($d015=r_o=0.015$) and a $\rho_+ = 0.025$ cut-off.

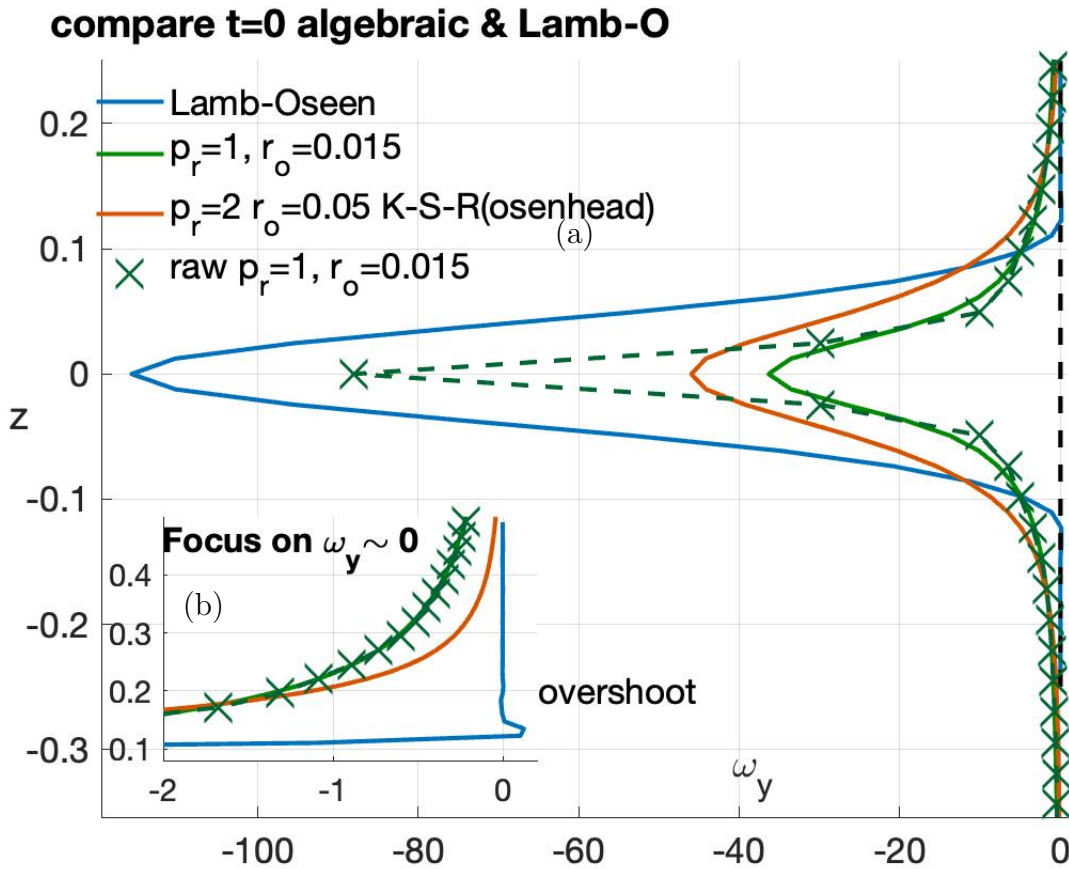


FIG. 5: $t=0$, $\omega_y(z)$ profiles through the $\min(\omega_y)$ of the $y=0$ $x-z$ plane for three of the cases from table I. All except one curve are taken after the non-solenoidal Fourier components have been removed. The profiles are for the $r_o=0.05$ Lamb-Oseen case (10) (Gd05) and two of the algebraic profiles that use the Rosenhead regularization (9). r2d05: $p_r=2$, $r_o=0.05$, referred to K-S-R, and r1d015: $p_r=1$, $r_o=0.015$. The other curve is the ‘raw’ $p_r=1$, $d=0.015$ curve, taken through its pre-Fourier-projected ω_y field. (a) The primary figure shows the full profiles in z . (b) The lower-left inset focuses upon $z > 0.1$ wings with small ω_y . Note the slight $\omega_y > 0$ overshoot at the boundaries of the Lamb-Oseen profile. This is the likely seed for the oscillations about $\omega_y = 0$ in figure 8.

Figure 5 compares the $t=0$ profiles of $\omega_y(z)$ for three of the profiles in table I. Each taken through the $\min(\omega_y)$ positions in their $y=0$, $x-z$ planes, as in figure 7. Both the main figure[†] and the ‘wings’ inset show that all

of the $t = 0$ algebraic profiles have smooth extended wings that never overshoot the $\omega_y = 0$ axis. In contrast, on the outer edge of the Lamb-Oseen profile there is some overshoot. Consistent with what has been seen before when Gaussian-like profiles are used for anti-parallel reconnection [7, 9].

The source of the Lamb-Oseen overshoot arises from the combined effects of the steepness of the outer edge of the L-O profile and a limitation of the algorithm (here and [3]) that is used map the $\omega_{\text{raw}}(\rho)$ field onto the Cartesian mesh in step 3). The mapping problem arises when the directions $\hat{\omega}$ of neighboring mesh points come from different positions on the centerline. Common when the distance ρ from the centerline is large. The steepness problem arises when finite $|\omega|$ points are next to points with $|\omega| \approx 0$. The mapped field sees these as finite jumps. Combined, in step 4) the projection of the mapped field can generate overshoots to negative values on the profile's edge. Overshoots whose magnitude is a function of the curvature of the centerline and the outer, $\rho \sim \rho^+$, steepness of $|\omega|(\rho)$.

It has been claimed that a curved coordinate system that accommodates internal twist [13] can yield divergence-free fields. That is the trajectory (8) used here, with zero internal twist and because the vortices are thinner than in my earlier papers, trajectory source points $\mathbf{x}(\phi)$ are adjacent for neighbouring \mathbf{x} , so that the raw vorticity fields are divergence-free. However, these are not the $t = 0$ initial fields of the simulations. This is because the profiles have sharp cut-offs at $\rho = \rho_+$ and when imported into a Fourier code, those interfaces generate Gibbs fluctuations. Leaving the investigator two choices. Either remove those fluctuations with a Fourier filter. Or continue with that background noise. Figure 1 quantifies that noise.

To demonstrate the importance of excessive steepness, one can decrease the maximum radius ρ^+ on an otherwise smooth profile. In section A a $\rho_+ = 0.025$ variant of the $p_r = 1, r_o = 0.015$ case is given whose $Z(t)$ and $\mathcal{H}(t)$ evolution has similarities with that of Lamb-Oseen in figure 1. Further implications of this could be the topic of another paper.

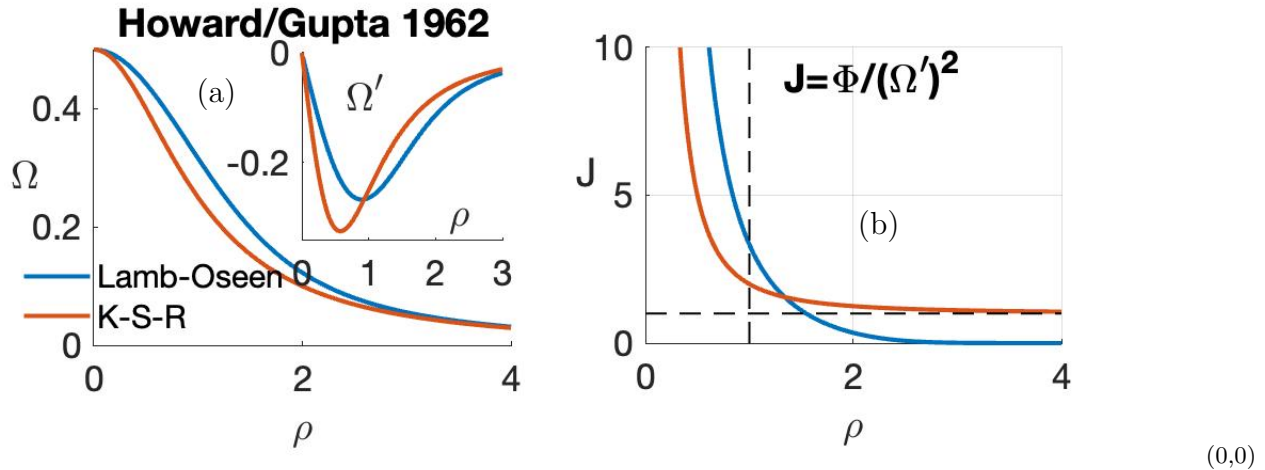


FIG. 6: To show how stability is determined using the $t=0$ Richardson functions $J(\rho)$ (12) for the Lamb-Oseen (10) and K-S-R (9) profiles with $r_o = 1$. (a) First, their $\Omega(\rho)$ and $\Omega'(\rho)$ profiles are similar. (b) What is important is how $J(\rho)$ asymptotes as $\rho \rightarrow \infty$. For Lamb-Oseen its $J(\rho) \rightarrow 0$ from (15), suggesting instability. While K-S-R, it is almost always stable by (14) as $J(\rho) \rightarrow r_o^2$, finite.

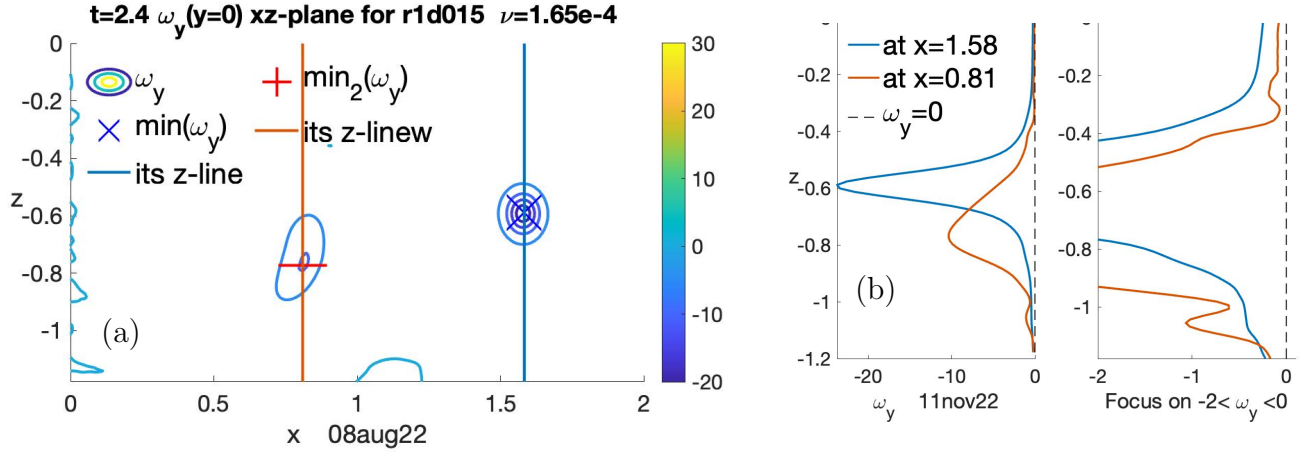


FIG. 7: ω_y at $t = 2.4$ on the $y = 0$, $x - z$ plane from algebraic case r1d015 with $p_r = 1$ and $r_o = 0.015$ (9). (a) Contour plot with local $\min(\omega_y)$ indicated. $|\omega_y| \sim 0$ contours do not appear. (b) $\omega_y(z)$ profiles through those minima at $x = 1.58$ and $x = 0.81$. First full $\omega_y(z)$, then focus on small ω_y . Contours and profiles at $t = 1.2$ are similar.

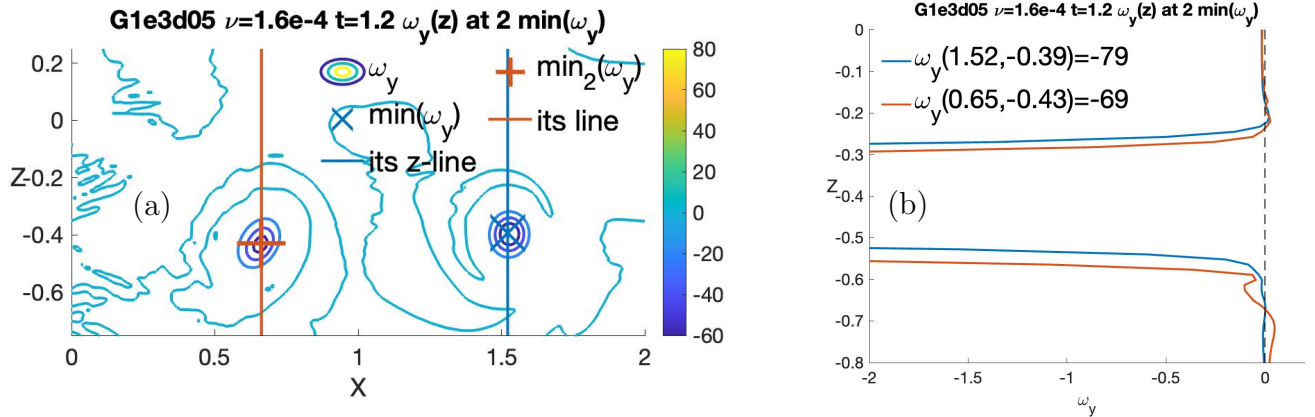


FIG. 8: ω_y at $t = 1.2$ on the $y = 0$, $x - z$ plane from the Lamb-Oseen profile (10) Gd05 calculation. (a) Contour plot with local $\min(\omega_y)$ indicated. A few $|\omega_y| \sim 0.001$ contours are included. (b) $\omega_y(z)$ profiles through those minima at $x = 1.52$ and $x = 0.65$. The positive overshoots of $\omega_y(z)$ show the magnitude of the $|\omega_y| \sim 0$ contours on the left.
† Note that the $y = 0$, $x - z$ plane negative ω_y extrema are not at the positions of the global $\max(|\omega|)$ for these fields.

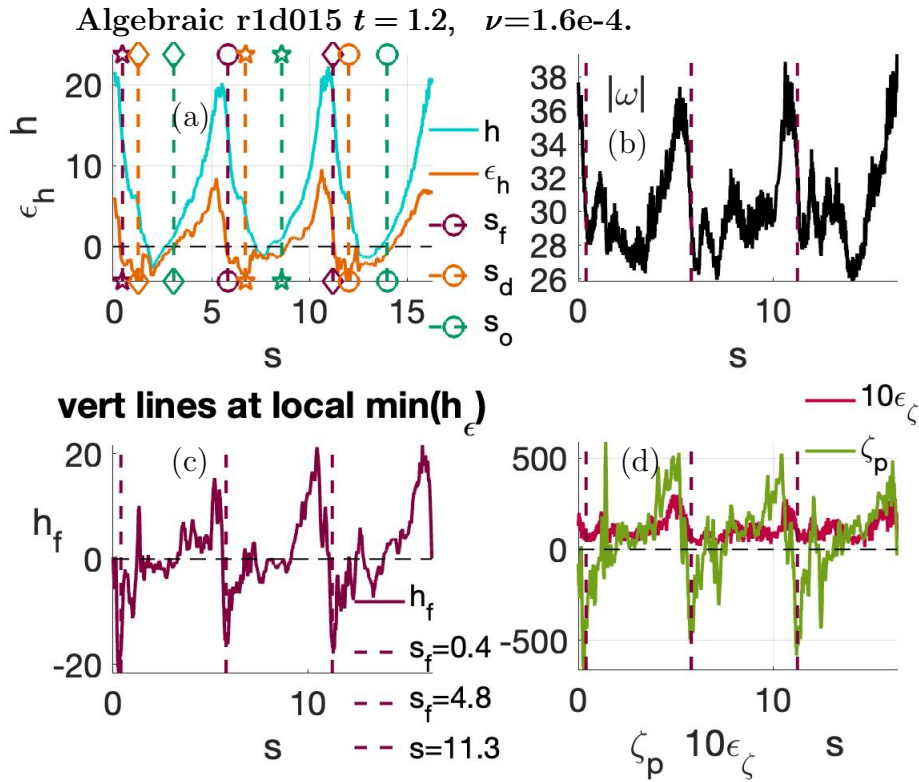


FIG. 9: $t = 1.2$ centerline budget profiles for algebraic case r1d015, $p_r = 1$ with $r_o = 0.015$, $\nu = 1.6e-4$ of h , ϵ_h , $|\omega|$, h_f , ϵ_ζ and ζ_p . (a) h and ϵ_h (6). (b) $|\omega|$. (c) h_f . (d) Production ζ_p and dissipation of ϵ_ζ of the enstrophy (5). Each frame has three vertical maroon lines at the s_f positions of the local min(h_f). Frame (a) has two additional sets: s_d positions of the local min(ϵ_h); s_o positions that oppose the s_f . All of the algebraic $0.4 < t \lesssim 2.4$ budget profiles are similar to these.

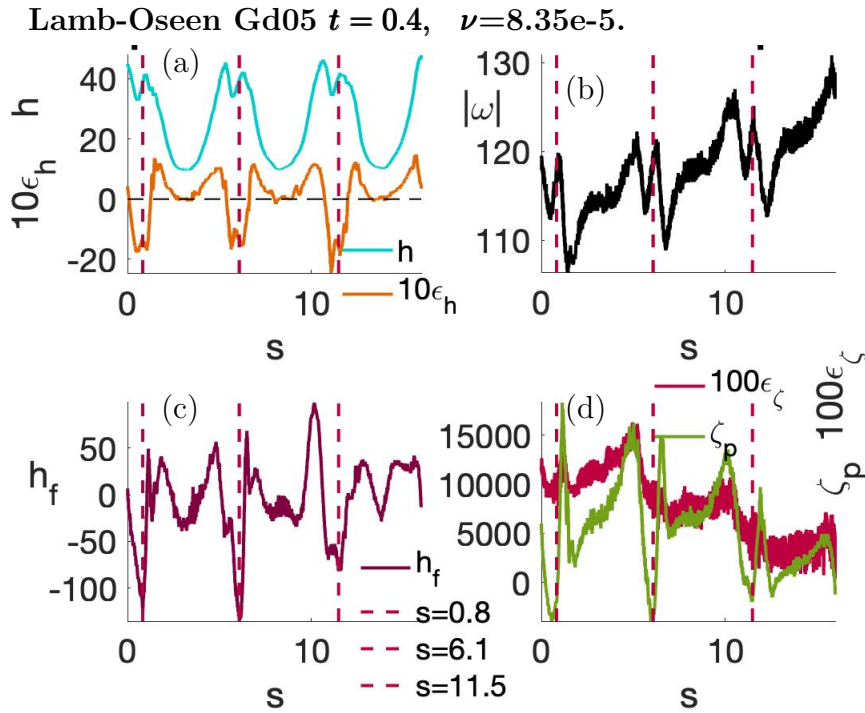


FIG. 10: Early $t=0.4$ Lamb-Oseen $r_o = 0.05$ centerline budget profiles of h , ϵ_h , $|\omega|$, h_f , ϵ_ζ and ζ_p . These are similar, but not identical, to the algebraic profiles at $t=1.2$ in figure 9. Significant positions: (c) s_f positions of local min(h_f). These are co-located with: (a) Local max(h) and min(ϵ_h). (b) Secondary local max $|\omega|$. (d) Local min(ζ_p), meaning at points of maximum centerline compression.

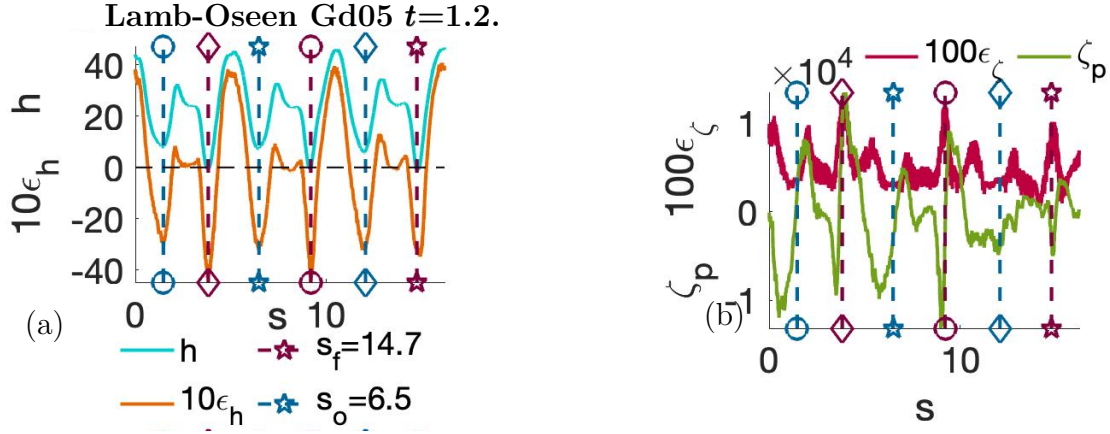


FIG. 11: $t = 1.2$ $r_o = 0.05$ Lamb-Oseen budget profiles. These are very different than the $t = 1.2$ algebraic budget profiles in figure 9. In (a) there are six positions with strong negative helicity dissipation, local $\min(\epsilon_h)$ and local $\min(h)$. The positions are separated into two sets of three. The s_f in maroon are at the strongest $\min(\epsilon_h)$, adjacent to the local $\min(h_f)$ (h_f panel is not shown). The s_o in turquoise are the points that oppose the s_f in 3D figure 4. In (b), all six positions are at very large positive gradients of ζ_p between local $\min(\zeta_p)$ and $\max(\zeta_p)$. Strong local $\min(\zeta_p)$ means strong local centerline compression. The s_f are also at $\max(\epsilon_\zeta)$ positions, maxima of the enstrophy dissipation.

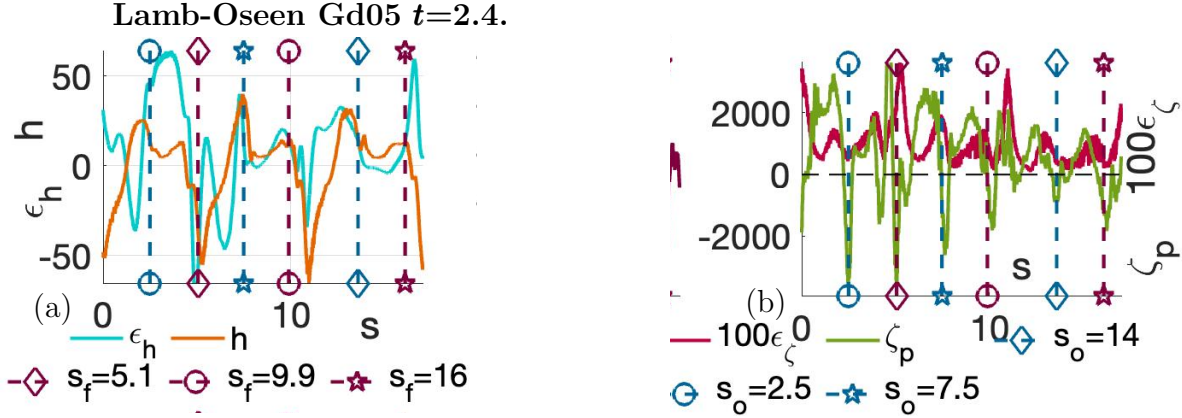


FIG. 12: $t = 2.4$ $r_o = 0.05$ Lamb-Oseen centerline budget profiles. (a) $h(s)$, $\epsilon_h(s)$, s_f (maroon) for local $\min(h_f)$ and the s_f 's opposing s_o (turquoise) are marked. The $\epsilon_h(s)$ profiles are three-fold symmetric again and more like the algebraic profiles at $t = 1.2$ and $t = 2.4$ and Lamb-Oseen at $t = 0.4$. (b) However, there are still six positions of local $\min(\zeta_p) < 0$ compression: The three s_f and three s_o . Having this many local compression locations is why the post-reconnection Lamb-Oseen vortex structures in section III C are braids, not the sheets generated by the algebraic profiles.

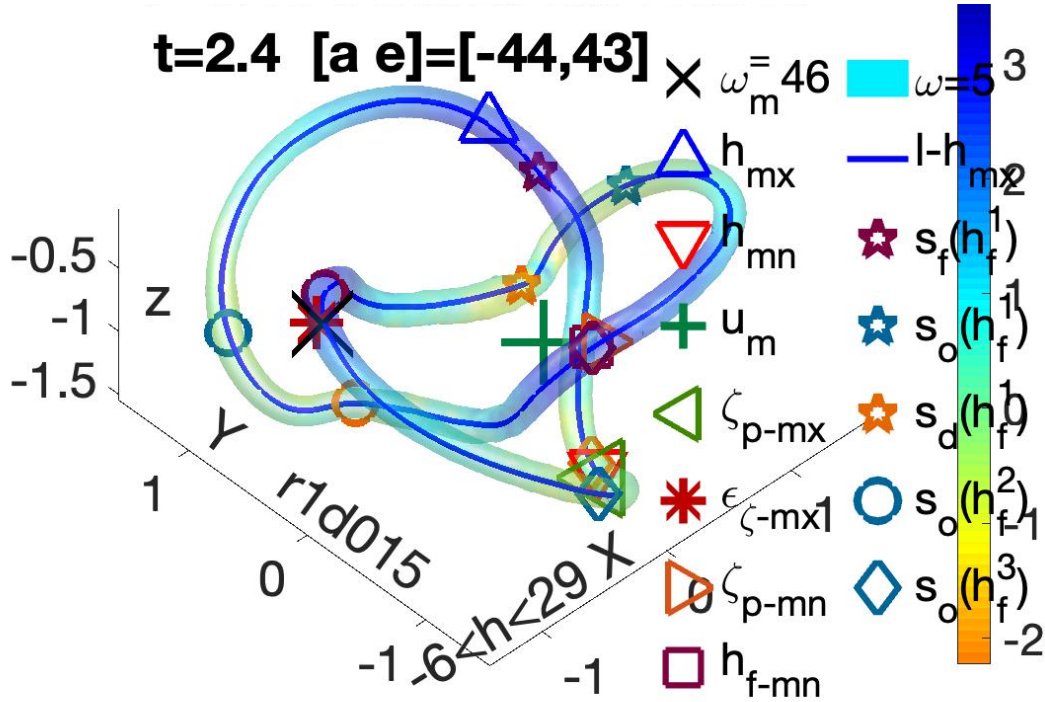


FIG. 13: A $t = 2.4$ mapped-helicity ω -isosurface from the r1d015 $p_r = 1, r_o = 0.015$ algebraic (9) calculation at the beginning of the initial phase of reconnection. Symbols (from legend) show the three-dimensional positions of the basic u, ω and h extrema as well as extrema from the entropy and helicity budget equations (5,6). Plus, from their centerline positions in figure 14, the s_f (maroon) positions of local $\min(h_f)$, the s_o (turquoise) positions that oppose the s_f and the s_d (yellow) positions of the local $\min(\epsilon_h)$. Each in sets of three associated with the 1st, 2nd and 3rd local centerline $\min(h_f)$ positions. There is a cluster of $\omega_m(\mathbf{X}), \max(\epsilon_\zeta)$ and $s_f(h_f^2) = 5.9$ on the left. Another cluster is next to u_m with $\min(h_f), \min(\zeta_p)$ and $s_f(h_f^3) = 11.7$. And one at the bottom with $\min(h)$ and $\max(\zeta_p)$ with $s_d(h_f^3) = 2.3$ and $s_o = 3.2$, both \diamond 's. The s_d and s_o with the same symbols are approaching one another on the same centerline spans of the trefoil. The best diagnostic for the Biot-Savart evolution of the vortex centerlines over this period is the separation of the three color-coded \circ 's on the left from $t = 1.2$, to 2.4 then 3.6.

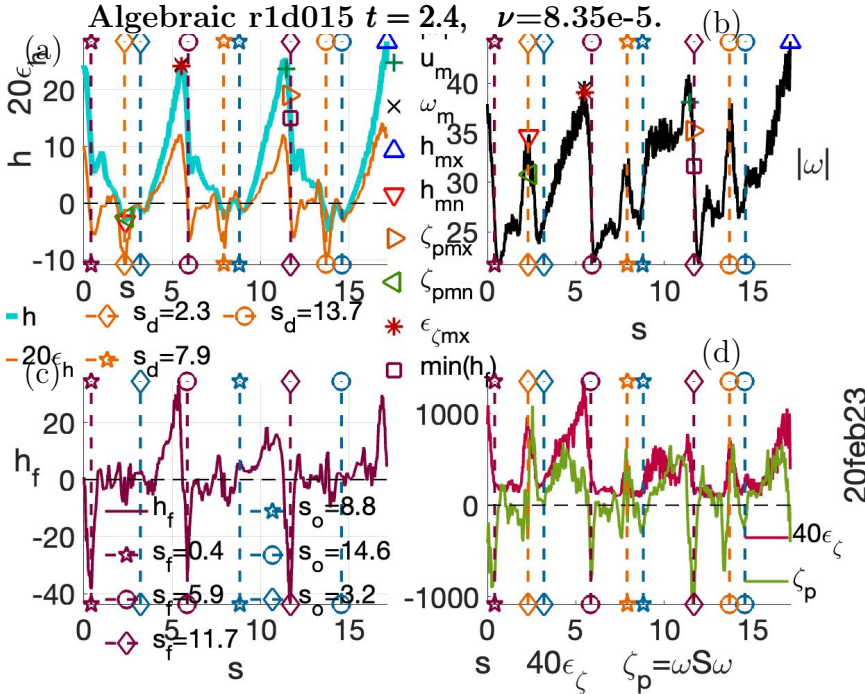


FIG. 14: Vorticity centerline budget profiles at $t = 2.4$ of $h, \epsilon_h, |\omega|, h_f, \epsilon_\zeta$ and ζ_p , case r1d015. Added to each panel are three sets of three vertical lines. Maroon lines at the local $\min(h_f)$. Yellow for local $\min(\epsilon_h)$ and turquoise for the s_o , the points opposing the s_f . The s_f points are on one side of each reconnection, with the $s_d - s_o$ zones representing the other side of those reconnections.

B. Rayleigh stability criterion

The stability of different core profiles $\omega(\rho)$ can be determined using the $J(\rho)$ (12) stability functions. The $J(\rho)$ are a type of Richardson number and derived for columnar vortices [14] by extending an earlier result for shears on boundary layers.

Recent analysis [15] that determines and uses the $J(\rho)$ begins with the azimuthal profiles of the velocity $u(\rho)$, vorticity $\omega(\rho)$ and the pressure p :

$$u = V(\rho)e_\theta, \quad \omega = W(\rho)e_z, \quad p = P(\rho). \quad (11)$$

P is determined up to an additive constant by centrifugal balance $rP'(\rho) = V^2(\rho)$. Then by introducing, the angular velocity $\Omega(\rho) = V(\rho)/\rho$ and $\Phi(\rho) = 2\Omega(\rho)W(\rho) = -P$, one can define these C^∞ and C^1 functions:

$$\Phi(\rho) = 2\Omega(\rho)\omega(\rho) \quad \text{and} \quad J(\rho) = \frac{\Phi(\rho)}{\Omega'(\rho)^2}, \quad \rho > 0. \quad (12)$$

Next, consider a small, but not tiny, perturbation of one Fourier mode:

$$\mathbf{u}(\rho, \theta, z, t) = u_{m,k}(\rho, t)e^{im\theta}e^{ikz}, \quad \omega(\rho, \theta, z, t) = \omega_{m,k}(\rho, t)e^{im\theta}e^{ikz}, \quad (13)$$

stability is determined by

$$\frac{k^2}{m^2}J(\rho) \geq \frac{1}{4} \quad \text{for all } \rho > 0 \quad (14)$$

Figure 6 shows $J(\rho)$, and how it is determined, for the Lamb-Oseen (10) and $p_r = 2$ algebraic (9) profiles for the same $\omega_o = 1$ and $r_o = 1$. What is important are their different $\rho \rightarrow \infty$ behavior. For the Lamb-Oseen profile

$$J_G(\rho) \rightarrow \frac{\rho^4}{r_o^2}e^{-(\rho/r_o)^2} \rightarrow 0, \quad (15)$$

implying that the inequality (14) is always violated as $r \rightarrow \infty$.

Whereas for the K-S-R $p_r = 2$ algebraic profile,

$$\frac{k^2}{m^2}J(\rho) \rightarrow \frac{(k^2 r_o^2)}{m^2} \quad \text{as } \rho \rightarrow \infty. \quad (16)$$

This says that unless m is large for $kr_o \sim 1$, that is its azimuthal wavelength is small, then for all ρ , $(k^2/m^2)J(\rho) \geq \frac{1}{4}$ can be satisfied. With an example of small being the Lamb-Oseen perturbation in the inset of figure 5, probably generated by the solenoidal projection in initialization step 4 in section II A.

Can the respective algebraic and Lamb-Oseen $J(\rho)$ stability curves in figure 6 foretell whether their evolution diverges at early times? The first test in figures 7 (r1d015, $t = 2.4$) and 8 (Gd05 $t = 1.2$). considers vertical profiles of ω_y taken though $y = 0$, $x - z$ slices.

For K-S-R, $J(\rho) \rightarrow r_o^2 > 0$, so stability is expected if m is large. And demonstrated by the ω_y contours in figure 7. And for Lamb-Oseen $J(\rho) \rightarrow 0 (< \frac{1}{4})$ and because there is a small perturbation, instability is possible. And demonstrated by the irregular $\omega_y \sim 0$ contours in figure 8. What is less clear for Lamb-Oseen is how tiny the perturbations must be to create instability [15]. As discussed in section IV B.

C. Effect of being stable or unstable

Do the stability differences indicated by figures 6, 7 and 8 yield differences in the subsequent evolution of the Lamb-Oseen and algebraic cases?

One difference between the respective $x - z$ slices (figures 7 and 8) is that the algebraic contours in figure 7 do not generate oppositely-signed contours. In contrast, Lamb-Oseen in figure 8 does: as shown by the $|\omega_y| \sim 0$ contours and the $\omega_y(z)$ slice on the right. These fluctuations of oppositely-signed ω_y are a source of local interactions. Local interactions that could be the source for the $t = 1.2$ differences between the algebraic and Lamb-Oseen centerline budget profiles in figures 9, and 11 respectively. This is discussed further in section III A.

D. Mapping budgets terms onto centerline vortices

While single-color helicity isosurfaces [1] suggested that helicity has a role in reconnection, the mapped h -vorticity isosurfaces used by two 2021 trefoil papers [3, 4] are a better tool. In particular, small values of localized oppositely-signed helicity $h < 0$ indicated where reconnection was forming.

There are similar yellow to red $h < 0$ patches at $t = 1.2$ in figure 4. For both algebraic and Lamb-Oseen. And for all cases, up to $t = 3.6$ there are similar $h < 0$ patches on their inner, higher ω isosurfaces. However, are the observed $t \leq 3.6$ differences sufficient for identifying the origins of the post-reconnection differences in the evolution of the algebraic and Lamb-Oseen calculations? Given how small those $t \leq 3.6$ inner isosurface differences are, they are not.

Why are the surface helicities of the different cases qualitatively similar? Likely because before reconnection begins, similar long-range Biot-Savart terms dominate the surface helicity dynamics for all cases. Therefore, what is needed are new diagnostics related to what is within the isosurfaces to explain the major differences in the $T > 3.6$ enstrophy and helicity evolution in figures 1 and 2. Meaning another set of pre-reconnection diagnostics is required.

Because these are questions about the evolution of local helicity $h(\mathbf{x}, t)$, which is controlled by its budget equation (6), one alternative set of diagnostics is to instead map the primary terms from the enstrophy and helicity density budget equations (5,6) onto the isosurfaces. The variations of these terms upon the isosurfaces are very small, so are not useful for analysing the dynamics by themselves. However, this exercise indicated that the local variations are strongest near the centerlines.

Suggesting that a better way to visualize the budget terms would be to map them onto the vorticity centerlines directly, if the centerlines can be identified. If successful, this would provides us with an analysis tool that is both local (at a point) and global (between distant points on the centerline).

To identify centerlines one must first choose appropriate seed points $\mathbf{x}_\omega(0)$ within a vorticity isosurface, then trace the vortex lines emanating from those points using a streamline function, giving trajectories $\mathbf{x}_\omega \in \mathcal{C}$ obeying

$$\boldsymbol{\xi}_\omega(s) = \frac{d\mathbf{x}_\omega(s)}{ds} = \boldsymbol{\omega}(\mathbf{x}_\omega(s)), \quad \text{whose lengths are } L_\omega = \oint |\boldsymbol{\xi}_\omega(s)| ds. \quad (17)$$

In [2, 12] the position of the maximum vorticity was used as the seed. With more experience, it has been found that seeding at either maximum or minimum of helicity, then using $-\boldsymbol{\omega}(\mathbf{x})$ direction in (17), yields trajectories that stay within the observed isosurfaces. This is the practice in this paper.

In all cases, the trajectories do not close upon themselves perfectly, which is only relevant for determining the topological numbers, twist, helicity and self-linking as in earlier work [2, 12]. That is not an objective of this paper.

Once the trajectories have been defined, the profiles of important dynamical terms are mapped onto those curves to determine how those properties are related to one another.

Note that because these vortex lines are almost closed upon themselves, initially the integral of the stretching $u_{s,s} = d\mathbf{u}/ds \cdot \hat{\boldsymbol{\omega}}$ on the ω -line is identically zero:

$$\oint_0^{L_\omega} u_{s,s} ds = u(L_\omega) - u(0) \equiv 0. \quad (18)$$

Due to this, any stretching along this line at $t = 0$ is balanced by equal compression somewhere else. And for these vortices, that compression also immediately yields an increase in the local enstrophy dissipation and negative helicity dissipation rates, ϵ_ζ and $-\epsilon_h$. As well as a very early decrease in the enstrophy and increase in the helicity: $dZ/dt|_{t=0} < 0$ and $d\mathcal{H}/dt|_{t=0} > 0$ as seen in figures 1 (Lamb-Oseen) and 2 (algebraic). More for the larger ν Lamb-Oseen calculations than the others.

E. Using these tools as time progresses.

The six terms from enstrophy and helicity budget terms that are mapped onto the centerlines are arranged into four panels:

- a) The helicity density h (cyan) and its dissipation rate ϵ_h (yellow).
- b) The vorticity magnitude $|\omega| = \sqrt{\zeta}$ (black).
- c) Helicity flux h_f (maroon), which includes a pressure gradient.
- d) Enstrophy density dissipation ϵ_ζ (red) and production ζ_p (lime).

All four panels appear in figures 9, 10, 14 and 18. For figures 11 (Gd05, $t = 1.2$), 12 (Gd05, $t = 2.4$) and 15 (r1d015, $t = 3.6$), some panels are not shown. In particular panel b) with $|\omega|$ is not shown because its s -profile closely follows that for the helicity h .

Figures with all, or most, of these six mapped terms are teamed with relevant three-dimensional helicity-mapped vorticity isosurfaces. The following markers indicate the locations of the primary extrema in three-dimensional space:

$$\omega_m = \|\omega\|_\infty \mathbf{X} \text{ (black); } \max(h) \Delta \text{ (blue); } \min(h) \nabla \text{ (red); } \max(u) + \text{ (green).}$$

- The additional global extrema from the budget equations are:

$$\max(\zeta_p) \blacktriangleleft \text{ (JungleGreen); } \min(\zeta_p) \blacktriangleright \text{ (RedOrange);}$$

$$\max(\epsilon_\zeta) * \text{ (VioletRed); } \min(h_f) \square \text{ (Maroon).}$$

- To identify relationships between the budget terms on the four panels, sets of three-fold symmetric dashed vertical lines are added at significant positions to allow comparisons between panels. The choice of vertical lines changes over time.

- At early times when transport along the vortices is most important, the local extrema of negative helicity transport $\min(h_f)$ positions are the best, and are identified by these marks, with vertical lines.:

- **Maroon** s_f indicate the positions of the local $\min(h_f)$ with these symbols:

- \star star,
- \diamond diamond,
- \circ circle.

- **Yellow** The s_d positions for local $\min(\epsilon_h)$ are important when reconnection is, or will be, forming.

- **Turquoise** is used for the s_o/s_o^+ positions opposing (\min or $\max=+$) extrema of the helicity flux h_f . That is the s_o/s_o^+ oppose in 3D the s_f/s_f^+ respectively. Each s_o/s_o^+ is separated from its s_f/s_f^+ -position by approximately $\Delta s = L_\omega/2$ along the centerline, where $L_\omega/2$ is half the length of the centerline trajectory (17).

- For algebraic case r1d015: At $t = 2.4$ in figures 13,14 the $s_o(h_f)$ that oppose the s_f are near s_d with local $\min(\epsilon_h)$.
- For $t = 3.6$ is transitional with the s_f and s_d in figure 15 being equally important as they mark the opposite sides of each developing reconnection site.

- **Green** is for the three-fold s_g points opposing the s_d local $\min(\epsilon_h)$ points.

- For $t = 4.8 > t_r = 4$ the s_d and s_g mark where there is active reconnection.

- For **Lamb-Oseen** $t = 1.2$ and 2.4 in figures 11, 12 the s_f and s_o mark where reconnection will form.

- For Lamb-Oseen $t = 3.6$, reconnections are marked by pairs of local s_f^+ (in cobalt) and s_o^+ points in figures 18 and 17a. ◦ While the s_d and s_f are co-located and far from the active reconnection between the s_f^+ and s_o^+ .

These budget maps are used to determine the dynamical interplay between the enstrophy and helicity over the period leading to reconnection for the broadest $p_r = 1$ algebraic case r1d015 and Lamb-Oseen case Gd05. For the K-S-R, $p_r = 2$ cases in section III E, only the essential time evolution and mapped helicity isosurfaces are given.

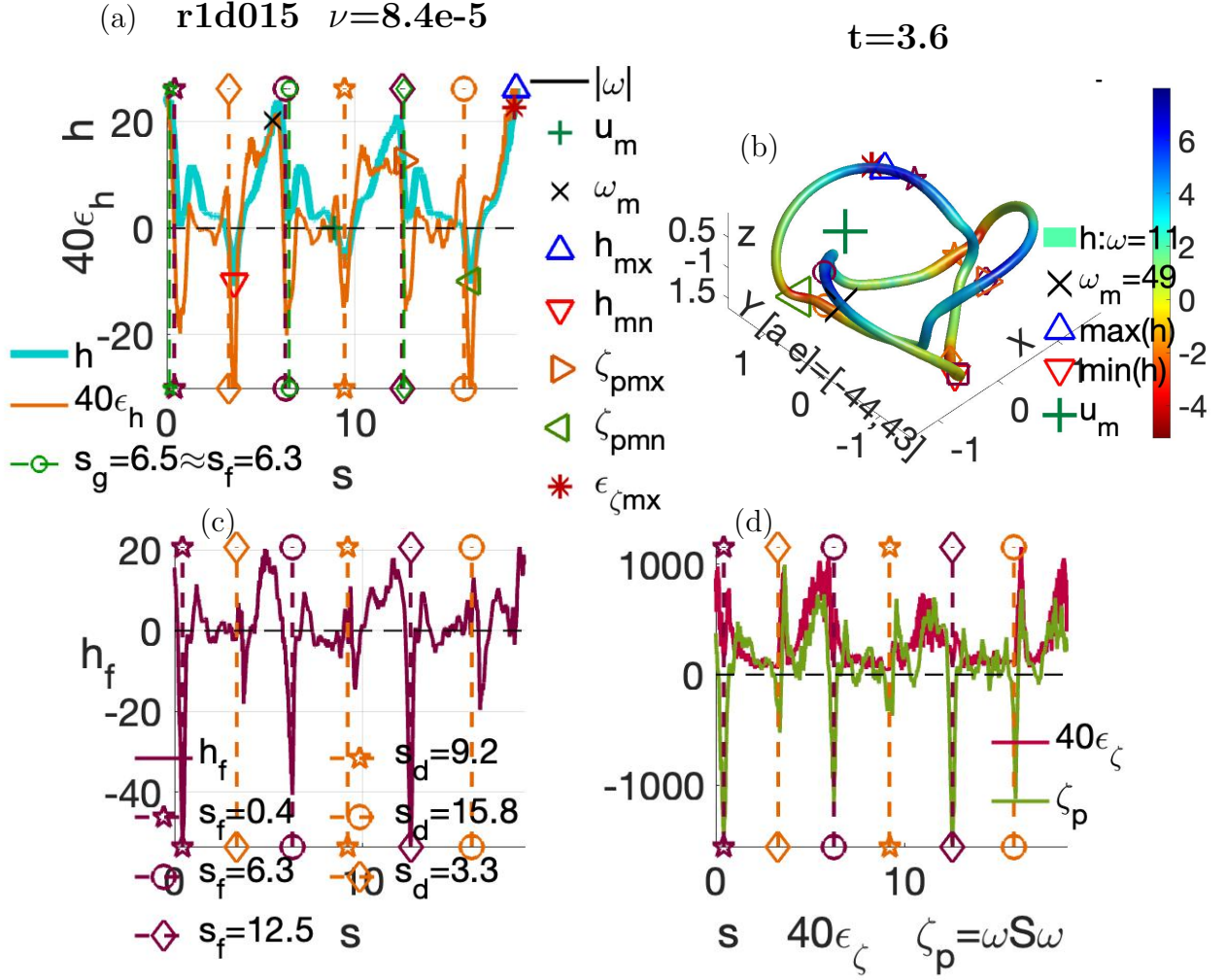


FIG. 15: Vorticity centerline profiles and an isosurface plot at $t = 3.6$ for case r1d015. Budget profiles: h , ϵ_h , h_f , ϵ_ζ and ζ_p , with added vertical dashed lines in each panel for these local positions: s_f (maroon, $\min(h_f)$); s_d (yellow, $\min(\epsilon_h)$); with in the upper-left panel s_g (green) for the s_d opposing points. The s_f are also at $\min(\zeta_p)$ and are at two of the $\max(\epsilon_\zeta)$ positions, local enstrophy dissipation peaks. The s_d are also at the local minima of the helicity $\min(h) < 0$, at cross-overs between secondary local $\min(\zeta_p)$ to $\max(\zeta_p)$ and at two of the local $\max(\epsilon_\zeta)$ positions. And are co-located with the opposing positions to the s_f . The s_g oppose the s_d and nearly coincide with the s_f . Where might reconnection form? The positioning of the s_f and s_d , plus their opposing points, suggests that reconnection would form between the s_f and s_d . Consequences: Local $\zeta_p < 0$ means that $du_s/ds < 0$ and due to incompressibility this implies the existence of stretching perpendicular to the vorticity at these points. The stretching needed to create the $h < 0$ vortex sheets. The upper-right panel uses a larger vorticity ($\omega = 0.2\omega_m$) isosurface than in figure 16 to show continuity with the earlier inner isosurface evolution. The labels for the auxiliary symbols are in figure 16.

III. RESULTS

The comparisons between helicity-mapped vorticity isosurfaces and the mapped centerline budget terms are presented chronologically:

III-A Early times for algebraic and Lamb-Oseen ($t = 0.4, 1.2$).

III-B Algebraic mid-reconnection $t=2.4$ and pre-reconnection $t = 3.6$, with the first appearance of extended $h < 0$ vortex sheets.

- After $t = 3.6$, the algebraic and Lamb-Oseen vortical structures and global evolution of $Z(t)$ and $\mathcal{H}(t)$ diverge, as shown by figures 1 and 2.

III-C $t \geq 3.6$ Lamb-Oseen Gd05. In figure 20 reconnection with vorticity bridges, localized sheets, then $t = 4.4$ braids.

III-D $t \geq 4.8$ algebraic reconnection with broad $h < 0$ ω -sheets leading to wrapping and accelerated enstrophy growth.

III-E Finally there is a short discussion of the K-S-R $p_r = 2$ r2d05 case.

A. Early times ($t = 0.4, 1.2$) profile dependent evolution and differences.

To begin, recall that for the $t = 1.2$ isosurfaces in figure 4 (cases r1d015, Gd05), the only clear difference between the frames is the position of the vorticity maximum ω_m . Can the centerline budget maps identify any greater differences at early times? First, the similarities at very early times are given, then the differences.

The centerline maps for the corresponding earliest times in figures 9, $t = 1.2$ algebraic, and 10, $t = 0.4$ Lamb-Oseen, are similar. While the strongest local $\max(h)$ and local $\max(|\omega|)$ are near to one another, other local extrema are associated with local $\min(h_f)$, the vortical helicity flux indicated by dashed maroon lines at local s_f . Positions of local helicity dissipation minima ($\min(\epsilon_h) < 0$) are near the s_f and the positions of local compression, $\min(\zeta_p) < 0$ are on the s_f . Suggesting that the dominant dynamics at these points is local compression with pinching at these points on the vortices.

However, starting at $t = 1.2$ the centerline dynamics of the two profiles diverge.

- For **algebraic case r1d015**, the alignments in figure 9 persist from $t = 0.4$ until the reconnection time of $t_r \sim 4$ is approached.
- However, for **Lamb-Oseen at $t = 1.2$** the corresponding Lamb-Oseen budgets in figure 11 are very different, showing six locations with roughly equivalent variations of the positive and negative helicity dissipation ϵ_h at six significant local $\min(h_f)$ positions, split into two sets of three, maroon s_f and turquoise s_o .

In figure 11a the s_f positions at local $\min(h_f) < 0$ (not shown) are also at the largest dips of $h \sim 0$ and the strongest local $\min(\epsilon_h)$. In (b), the s_f are not exactly on local $\min(\zeta_p)$, but on the adjacent large positive gradients and local enstrophy dissipation peaks: $\max(\epsilon_\zeta)$. These s_f can be viewed as one side of the developing reconnection sites.

The turquoise s_o positions that oppose the s_f positions in figure 4 are the other side of the developing reconnections. They are also secondary local $\min(\epsilon_h)$, secondary local dips in h and near secondary local $\min(\zeta_p)$. Meaning that all six positions (the s_f and s_o) are sitting at or near local compressive $\min(\zeta_p) < 0$.

Having multiple points of local compression at an early time has a significant effect upon the the enstrophy growth (or decay). At $t = 1.2$ and 2.4, the localized pinching enhances the localized dissipation of both helicity ϵ_h and enstrophy ϵ_ζ , which also suppresses the ζ_p terms needed to enhance enstrophy growth: before that growth has even begun. A likely source of this localization of the dynamics is the interactions between the primary vorticity and the oppositely-signed flotsam seen in figure 8. That is, the origin of this localized dynamics is the amplification of that noise by instability, as previously suggested [9] and discussed here in section IIB.

The $t = 2.4$ Lamb-Oseen centerline budget profiles in figure 12 show some return to normal. They have similarities with the $t = 0.4$ Lamb-Oseen profiles in figure 10 and the pre-reconnection algebraic profiles for $t \leq 3.6$. While there are only three local $\min(\epsilon_h)$ and $\min(h_f)$, in the right frame there still is strong compression with local $\min(\zeta_p) < 0$ at all six of the former ($t = 1.2$) $\min(h_f)$ positions: The three current ($t = 2.4$) s_f positions and their three s_o opposing positions. In addition, the magnitudes of the enstrophy production ζ_p and dissipation ϵ_ζ terms are tempered, being a factor of 5 less than at $t = 1.2$.

This localized dynamics is only temporarily stronger than the long-range Biot-Savart interactions: Once that dynamics dissipates, the Biot-Savart interactions again control the large scales and the evolution of the centerline trajectory. However, the dynamics along the centerlines is permanently affected. When reconnection bridges do form, with some enstrophy growth, it is entirely concentrated at the locations in figure 11. Not over the entire trefoil. With rapid post-reconnection dissipation of the vorticity in the bridges, leading to divergent evolution of the enstrophy $Z(t)$ and the helicity $\mathcal{H}(t)$. Explained further in section III C.

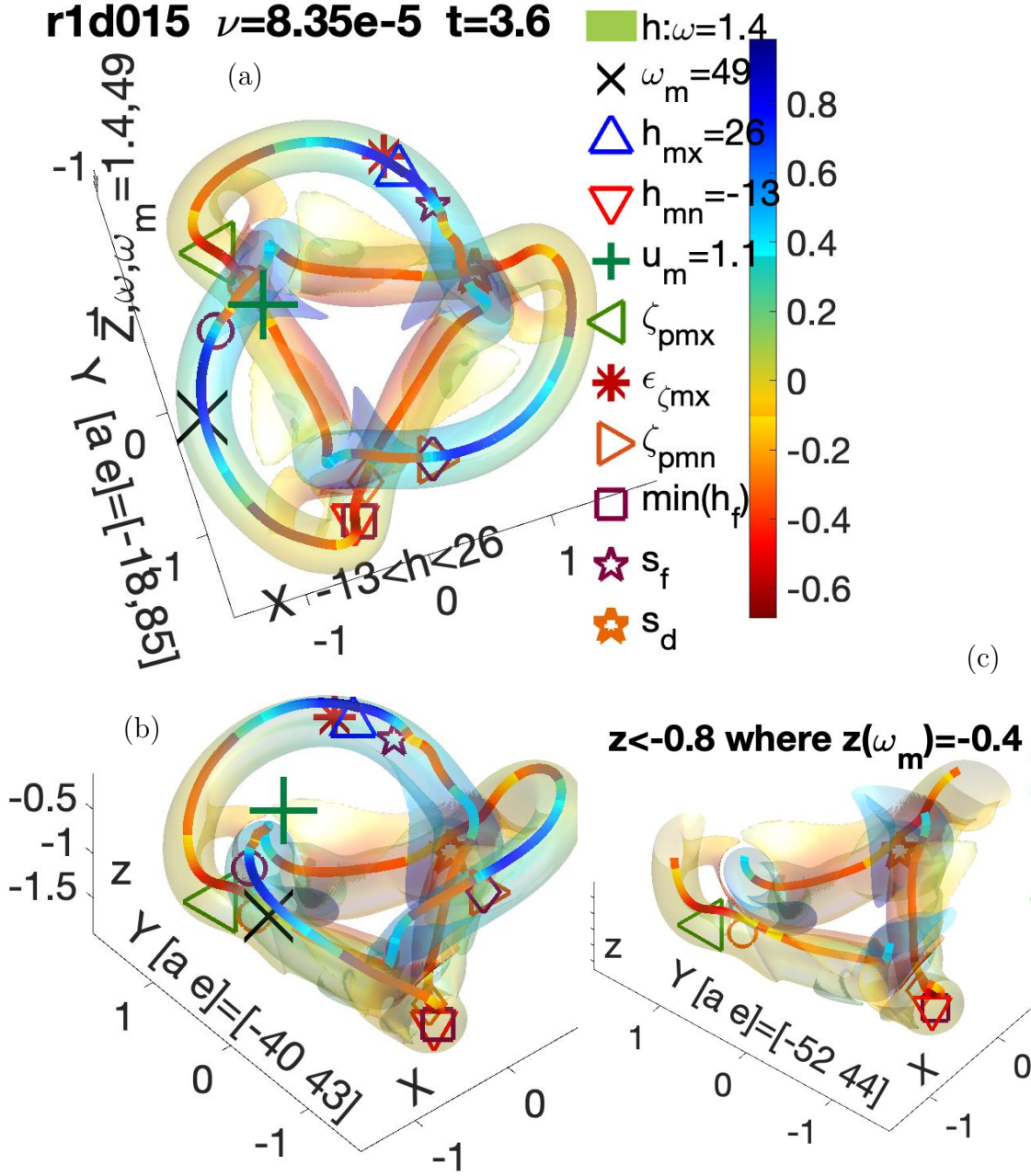


FIG. 16: A $t = 3.6$ mapped-helicity ω -isosurface for case r1d015 with a color-coded centerline from three-perspectives. Symbols show the three-dimensional positions of the basic u , ω and h extrema as well as extrema from the enstrophy and helicity budget equations (5,6). Plus the s_f (maroon) positions of local $\min(h_f)$ and the s_d (yellow) positions of the local $\min(\epsilon_h)$, which also oppose the s_f (the s_o in figure 15). (a) is a plan view perspective with faint $h \lesssim 0$ yellow sheets extending out from lower reddish ring. Then two sideviews from the same. (b) shows the entire domain. (c) shows only $z < -0.8$ with the lower emerging ring, below the \mathbf{X} position of ω_m at $(x, y, z) = (-1.37, -0.25, -0.39)$. The centerline vortex has mapped helicity ranging from red ($h = -13$) to blue ($h = 26$). By using a small $\omega \sim 1.4 \sim 0.03\omega_m$ vorticity isosurface, a gradation can be seen in the lower $h < 0$ zone from a red $h \sim -0.4$ inward facing half to the yellow-green $h \lesssim 0$ outward half. This is the first step in the formation of the yellow negative helicity $h \lesssim 0$ vortex sheets at later times. It is rotated to the right to give some 3D perspective of the yellow lobes on the right and above.

B. Mid-reconnection $t=2.4, 3.6$, with algebraic spawning sheets.

In the $t \leq 3.6$ period before reconnection begins, there are few differences between the inner, larger ω isosurfaces of cases r1d015 and Gd05. However, there are significant differences between their pre-reconnection budget profiles. Significant enough that for this mid-reconnection phase, the evolution of algebraic case r1d015 and that of Lamb-Oseen case Gd015 are considered separately. Algebraic in this section and Lamb-Oseen in section III C.

To follow the evolution of the r1d015 isosurfaces and budgets between $t = 1.2, 2.4$ and 3.6 , three sets of three-fold positions are indicated on each: s_f at local $\min(h_f)$; the s_d at local $\min(\epsilon_h)$; and points opposing either the s_f (the s_o) or the s_d (the s_g). These are in addition to the usual extrema: $\max|u|$, $\max|\omega|$, $\max(h)$, $\min(h)$, $\min(\epsilon_h)$, $\min(h_f)$, $\max(\epsilon_\zeta)$ and the \min and $\max(\zeta_p)$. Once defined, the s_f , s_d and s_o/s_g can be used to follow the evolution of the isosurfaces and budget profiles of the r1d015 calculation at $t = 1.2, 2.4$ and 3.6 as follows:

- At the points of closest approach, the s_f and s_o , the isosurfaces are drawn together over time.
- At the same time, the s_d and s_g approach one another along the centerline until they coincide at $t = 3.6$.
- These locations can help identify where there are spans of $\epsilon_h < 0$ and $h < 0$ along the centerline. So that at $t = 2.4$ and 3.6 besides the local $\min(\epsilon_h) < 0$ at the s_d , there are also growing, smaller peaks of $\epsilon_h < 0$ next to the s_f and between the $s_f + s_d$ pairs, growing s -spans of $\epsilon_h \lesssim 0$. On both the isosurfaces and the centerlines as in figures 13 and 14a and 15a,b. With some $h \lesssim 0$ at the s_d .
- At $t = 3.6$ the s_o are co-located with the s_d . With the s_g nearly co-located with the s_f , as shown in figure 15a. And the spans of $\epsilon_h < 0$ and $h \lesssim 0$ from $t = 2.4$ are now concentrated at the s_d points, with $\epsilon_h < 0$ and $h < 0$ being particularly deep at those points. There is also local $\epsilon_h < 0$ at the s_f with $\epsilon_h \approx 0$ between the s_f the next s_d .
- For example $\epsilon_h \approx 0$ between $s_f=6.3$ and $s_d=9.2$. Another $\epsilon_h \approx 0$ that started at $t = 2.4$ with $20\epsilon_h < -5$ at $s_f=0.4$ to $s_d=2.3$ at $t = 3.6$ goes to $s_d=3.3$.
- These small patches of $h < 0$ and $\epsilon_h < 0$ on spans of the centerlines and inner isosurface are not evidence for $h < 0$ vortex sheets. The patches are even similar to Lamb-Oseen as reconnection at $t = 3.6$ in section III C. Instead, the patches of $\epsilon_h \lesssim 0$ could be evidence of where $h < 0$ vortex structures are being created.

How the $h < 0$ isosurface vorticity forms:

- **$h < 0$ formation.** While at $t = 2.4$ there are spans of $h(s) < 0$ in figure 14, this does not translate into significant \pm variations of h on the $t = 2.4$ isosurface or signs of vortex sheets. It is not until $t = 3.6$ that significant dips of $h < -5$ appear at the s_d locations. On both the centerline and the inner (large ω) isosurface in figure 15(a,b).
- What is new in 3D at $t = 3.6$ is extensive $h < 0$ on parts of the smaller vorticity magnitude outer isosurfaces in figure 16. Red for strong $h < 0$ along the red-coded centerline in the lower ($z < -0.8$) portion of the trefoil. And yellow $h \lesssim 0$ helicity on the other side of those isosurfaces, with faint signs of shed vorticity. A trend that continues to later times, as illustrated in figure 21 at $t = 4.8$.
- **Relation between $h < 0$ centerlines and isosurface zones.** The red on the isosurface is associated with the broader spans of centerline $\epsilon_h(s) \lesssim 0$ that connect the s_f and s_d local positions. Example: Follow the maroon $s_f \star$ through where the loops cross, then down to the yellow $s_d \diamond$. Or from the maroon $s_f \circ$ to the yellow $s_d \star$ underneath the maroon \star .
- With all corresponding to $\epsilon_h \sim 0$ spans between all six local $\min(\epsilon_h)$ at the s_f and s_d in figure 15a.
- The reddish $h < 0$ patches extend over roughly 2/3rds of these spans on the lower ($z < -0.7$) part of the isosurface.
- With the reddish zones smoothly transitioning into the yellowish, more sheet-like outer surfaces.
- This is illustrated further at $t = 4.8$ with the red patches in figures 21 and 23.
- Further $t = 3.6$ figures from different perspectives and different cropping levels will appear shortly. *Phy. Rev. Fluids* (accepted, 2023) *Sensitivity of trefoil vortex knots upon the initial vorticity profile*.

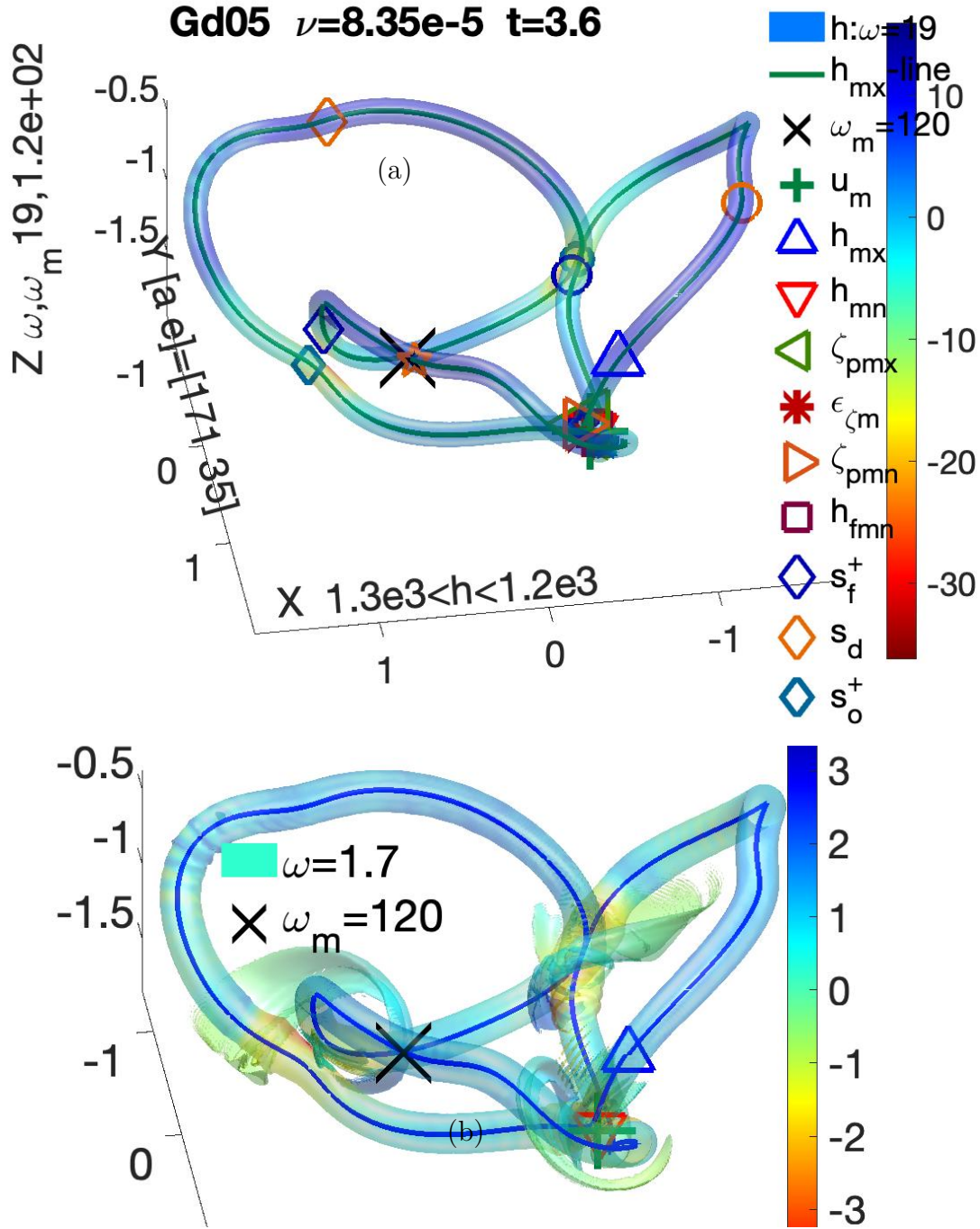


FIG. 17: Two $t = 3.6$ Lamb-Oseen isosurfaces with different vorticity thresholds. (a) The primary $\omega = 19$ isosurface is similar to the higher- ω algebraic isosurface in figure 15. Additional markers indicate the three-dimensional locations of the s_d (yellow), local $\min(\epsilon_h)$, s_f^+ (cobalt) for the local $\max(h_f)$ points and s_o^+ (turquoise), points opposing the s_f^+ that are also $\min(h) < 0$ and $\min(\zeta_p)$ points. Reconnection is commencing between the s_f^+ and s_o^+ points. The local s_d (yellow), $\min(\epsilon_h)$ sit in strongly positive $h > 0$ zones, not $h < 0$ as for the algebraic calculations or Lamb-Oseen for $t \leq 2.4$. (b) The vorticity of the second isosurface uses very small $\omega = 1.7$ to show that the outer edges of the isosurface are shedding sheets with slightly negative helicity.

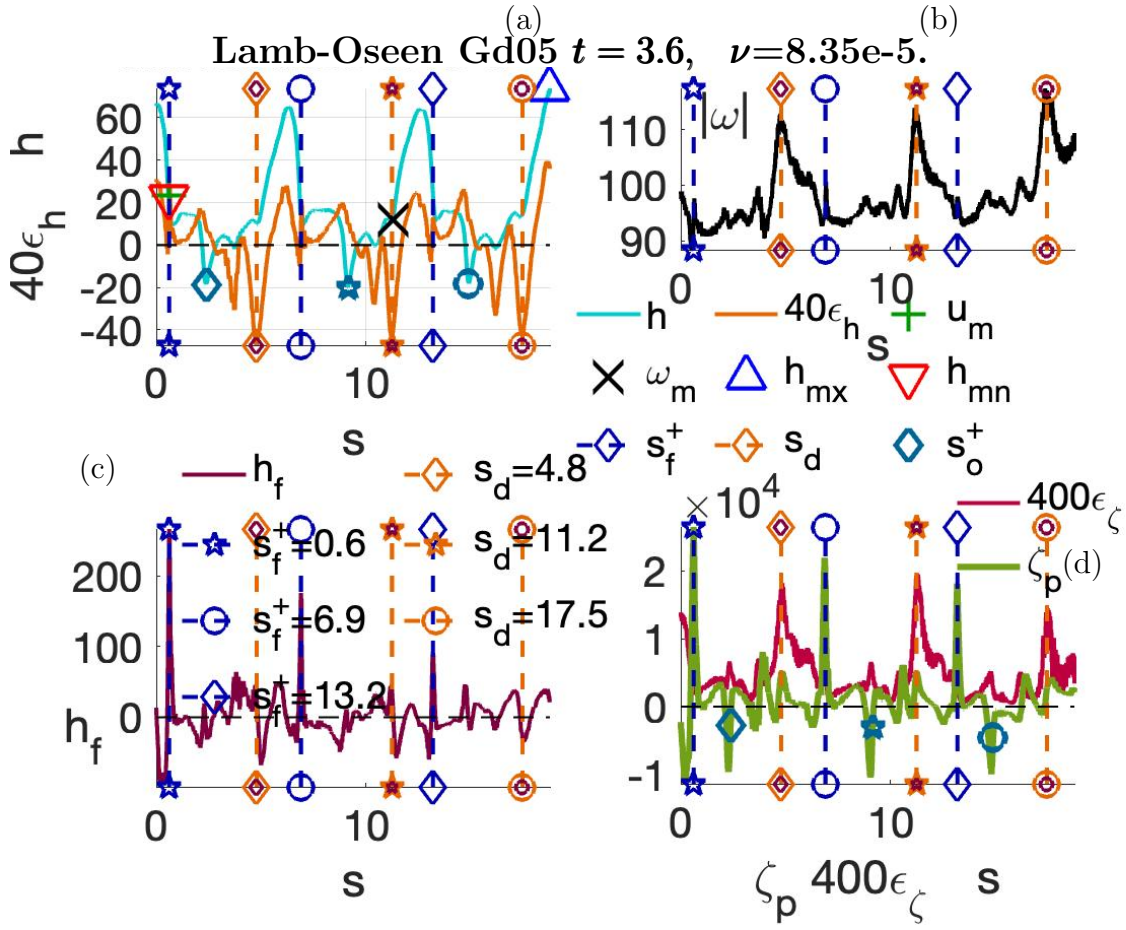


FIG. 18: $t = 3.6$ Lamb-Oseen (Gd05) (10) centerline budget profiles. The s_d (yellow/maroon) at local $\min(\epsilon_h)$ and co-located with local $\max(\epsilon_\zeta)$ and $\max(|\omega|)$, are in large $h > 0$ zones far from the reconnections. The s_f^+ (cobalt) are at local $\max(h_f)$ points and co-located with local $\max(\zeta_p)$ and secondary velocity minima. The s_o^+ (turquoise) points oppose the s_f^+ and are co-located with $\min(h) < 0$ and $\min(\zeta_p)$ points. Reconnection is commencing between the s_f^+ and their opposing s_o^+ points.

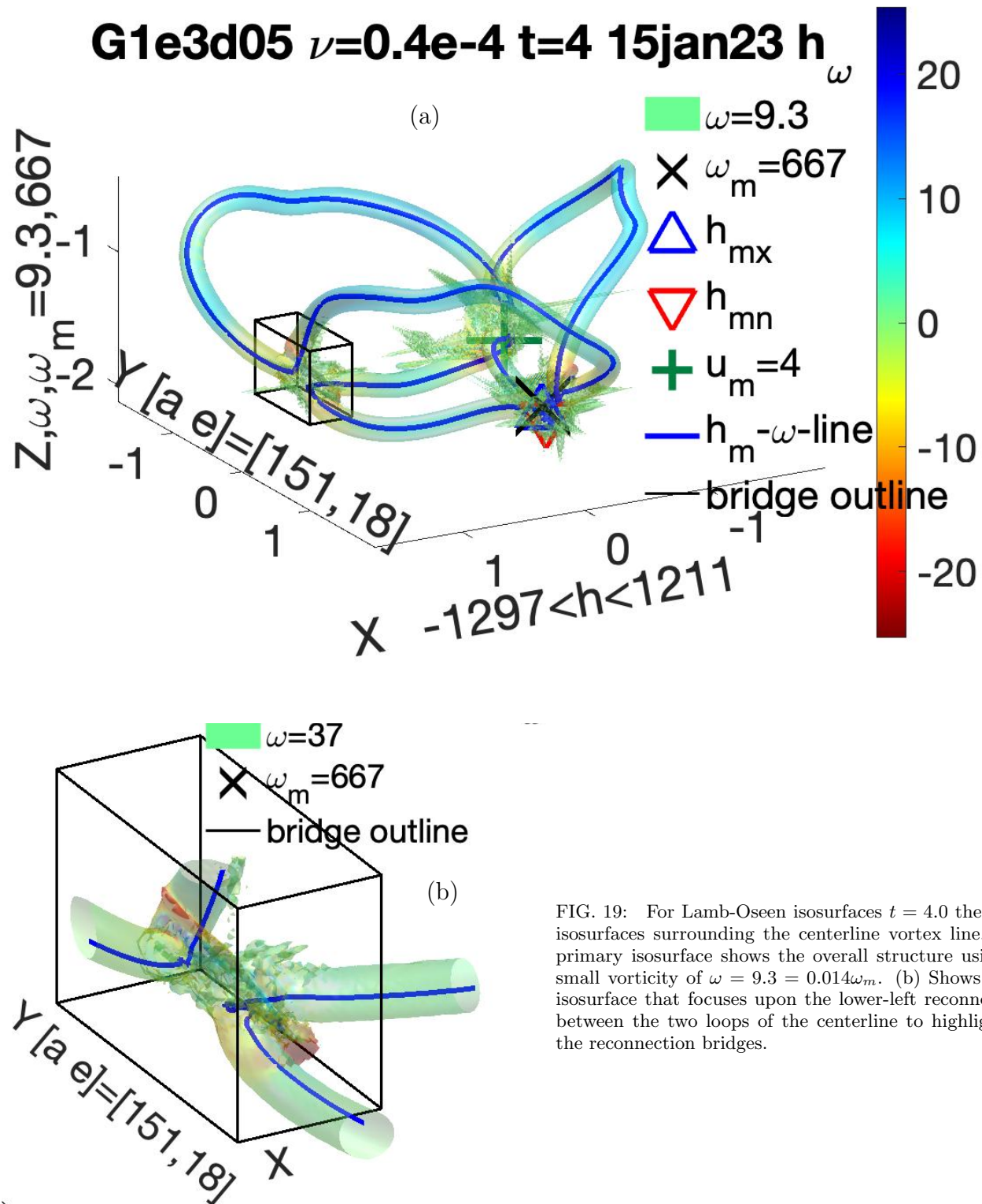


FIG. 19: For Lamb-Oseen isosurfaces $t = 4.0$ there are two isosurfaces surrounding the centerline vortex line. (a) The primary isosurface shows the overall structure using a very small vorticity of $\omega = 9.3 = 0.014\omega_m$. (b) Shows a $\omega = 37$ isosurface that focuses upon the lower-left reconnection site between the two loops of the centerline to highlight one of the reconnection bridges.

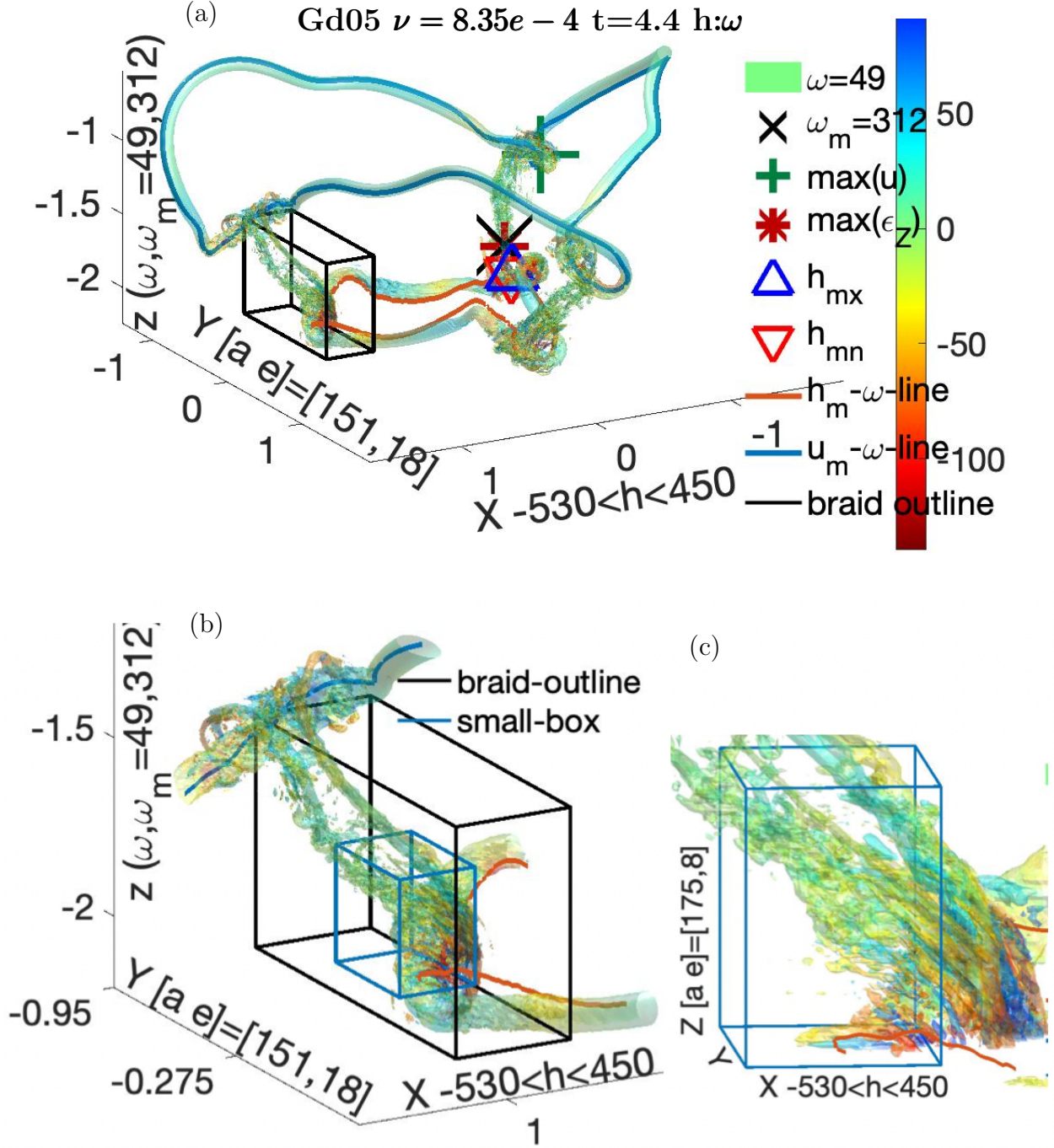


FIG. 20: $t = 4.4$ Lamb-Oseen isosurfaces. (a-c) Three views the isosurfaces, with the bottom two focusing upon the smallest structures. (a) The primary $t = 4.4$ isosurface shows the overall structure with $\omega = 49 = 0.015\omega_m (=312)$ to show how braids are forming from bridges, as seen for previous Lamb-Oseen calculations. (b) Shows full length of one of the double braids, including where it attaches to the new upper and lower vortex rings. Similar to $t = 4.29$ of figure 18 from [3]. (c) Focuses on one end as that double braid winds around the primary vortex.

C. Gaussian/Lamb-Oseen reconnection: braid formation.

In section III A, early divergence of $t = 1.2$ Lamb-Oseen budget profiles from the algebraic profiles was shown respectively in figures 11 (Gd05) and 9 (r1d015). Section gives the effect of that early divergent dynamics upon Lamb-Oseen as reconnection begins. Beginning at $t = 3.6$ with figures 17 and 18. $t = 3.6$ is the last time that a single centerline could be identified for case Gd05.

The Lamb-Oseen analysis ends with the $t = 4$ and 4.4 isosurfaces in figures 19 and 20. These show how the trefoil then breaks into two vortex rings, connected first by what could be described as bridges, then as braids.

The two Lamb-Oseen $t = 3.6$ isosurfaces in figure 17 are:

- (a) A primary, higher magnitude $\omega = 19$ isosurface that shows continuity with the earlier Biot-Savart evolution and has minimal differences with the $t = 3.6$ inner algebraic structure in figure 15.
- (b) The lower magnitude $\omega = 1.7$ isosurface shows how the Lamb-Oseen profile reconnection begins on the outer wings, with sheets shedding with some $h \lesssim 0$. These sheets with bits of $h \leq 0$ are localized around the reconnection points, unlike the broad $h < 0$ isosurface zones of the r1d015 algebraic trefoil in figure 16.

The $t = 3.6$ budget profiles and isosurfaces in figures 17 and 18 have three sets of primary local positional marks. s_d , s_f^+ and s_o^+ . Plus the s_f .

- The s_d in yellow (with embedded maroon s_f) are at local $\min(\epsilon_h) + \min(h_f)$ positions. The s_d are exactly on local $\max(|\omega|)$ and $\max(\epsilon_\zeta)$, the maximum enstrophy dissipation.
- The s_f^+ in cobalt are at the local $\max(h_f)$ and are coincident with local $\max(\zeta_p)$. Local $\zeta_p > 0$ implies stretching, suggesting that these positions could be the seeds for the bridges that form during reconnection.
- The third set of s_o^+ in turquoise are at the points opposing the s_f^+ . The s_o^+ are also local $\min(h)$ and $\min(\zeta_p)$, local compression, suggesting that there is pinching on the trefoil vortex at the other end of the nascent bridges.
- All consistent with active reconnection at these positions.
- What can the $t = 3.6$ markers tell us about the separation of the trefoil into two rings?
 - The cobalt $\max(h_f)$ s_f^+ points with large $\zeta_p > 0$ become one end of the bridges, with their opposing turquoise s_o^+ at the other end.
 - The s_d yellow $\min(\epsilon_h)$ points are on what becomes the upper (u) ring, with magnitudes $h_u > 0$.
 - The turquoise $s_o^+/\min(h)$ points become the lower (ℓ) ring, with some $h(s_o^+) < 0$ appearing on the localized vortex sheets in figure 17b, such as to the left of ω_m (\mathbf{X}).
- What develops out of this $t = 3.6$ state?
 - At $t = 4$ in figure 19, short, flattened bridges are generated as the trefoil is begins to separate into two rings.
 - The positions of ω_m , u_m , h_{mx} and h_{mn} are all on the bridges.
 - At $t = 4.4$, in figure 20, the new upper (blue) and lower (red) rings are separating, with each bridge splitting into two braids.
 - The positions of ω_m , h_{mx} and h_{mn} are on the the lower ring and u_m is on the upper ring.
- Figures 19 and 20 are roughly equivalent to the $Re = 12000$ figures at the same times for a previous trefoil calculations using Lamb-Oseen profiles [3]. Including the splitting of each bridge into two braids.
- So providing further Gaussian/Lamb-Oseen graphics and discussion in this paper is unnecessary.
- Summary of how the Lamb-Oseen budget profiles in figures 11, 12 and 18 can explain the evolution of the global enstrophy $Z(t)$ and the helicity $\mathcal{H}(t)$ in figure 1:
 - Starting at $t = 0$ when $\int ds \zeta_p \equiv 0$, for the spans with local compression, $\zeta_p < 0$, the viscous terms and ϵ_ζ are enhanced. Resulting in $Z(t)$ decreasing for at least short $t \gtrsim 0$ times for all cases and viscosities ν .
 - Between $t = 2.4$ and 3.6, the global enstrophy production and its dissipation rate are approximately equal to their centerline integrals: $Z_p = \int dV \zeta_p \sim \int ds \Gamma \zeta_p$ and $\epsilon_Z = \int dV \epsilon_\zeta \sim \int ds \Gamma \epsilon_\zeta$.

With Z_p and ϵ_Z roughly balancing one another in figures 12,18 ($t = 2.4, 3.6$), giving $dZ/dt = Z_p - \epsilon_Z \approx 0$ over the temporal span of $2.4 \leq t \leq 3.6$. And relatively steady $Z(t)$, enstrophy, over those times in figure 1.

- At $t = 3.6$ in figure 18, at the locations of positive, not negative, spikes in h_f , there are sharp positive spikes in the enstrophy production ζ_p .
- These spikes of $\zeta_p > 0$ continue through $t = 4$, generating the are brief enstrophy spurt in figure 1. This spurt is when the bridges form, shown in figures 17 and 19.
- Then as the strong centerline enstrophy dissipation ϵ_ζ in figure 18 takes over, the centerline spikes of local $h_f > 0$, $\zeta_p > 0$ and $\omega = \sqrt{\zeta}$ and ζ_p , are dissipated. Along with the temporally spikes of $Z(t)$ in figure 1.
- For $\mathcal{H}(t)$, except at $t \sim 1.2$ as in figure 11, its $t \leq 3.6$ evolution is dominated by the strongly localized negative helicity dissipation ϵ_h , which removes $h < 0$, thereby leading to increasing $\mathcal{H}(t) > 0$. After $t = 3.6$, as dissipation removes the small amounts of $h < 0$ associated with the bridges, $\mathcal{H}(t)$ increases further.

D. Algebraic reconnection scaling with $h < 0$ ω -sheets.

Due to the constraints imposed upon the calculations in this paper, three-fold symmetry and a $(2\pi)^3$ domain, it has been a surprise that the algebraic profile cases have generated this: Finite-time, finite energy dissipation ΔE_ϵ (1), as shown in figures 2 and 25 by the finite-time convergence of the dissipation rates $\epsilon(t) = \nu Z$ of the broadest profiles: cases r1d015 and r2d1. At least for a short range of viscosities. The evidence for finite ΔE_ϵ in the earlier perturbed trefoil calculations [2] could only be achieved by using very large domains.

Furthermore, for all of the algebraic profile calculations there are vortex sheets and convergent $\sqrt{\nu}Z$, such as in figure 3 (r1d015) and the examples in section III E. Although with profile dependent convergent times $t_x > t_r$.

What are the underlying structures and dynamics that allow the subsequent enstrophy growth to accelerate and form finite ΔE_ϵ for these cases? Figures 16 and 15 at $t = 3.6$ show where, and how, the conditions for generating negative helicity vortex sheets originate. This section extends that analysis to $t = 4.8$ to show how the sheets then expand and contribute to the enstrophy growth: growth that can lead to finite-time energy dissipation. Skipping the gradual changes at the intermediate times of $t = 4$ and $t = 4.4$. The important differences with the Lamb-Oseen calculation are also highlighted.

The three-dimensional structure at $t = 4.8$ is illustrated in figures 21 and 22 using several perspectives of two vorticity isosurfaces and red $h < 0$ hash marks. Mapped- h is on the broader isosurface with a lower vorticity: $\omega = 0.64 \approx 0.02\omega_m$. And a higher vorticity $\omega = 14$ monochrome isosurface that encases the centerline vortex. With the red hash marks indicating the $\epsilon_h \lesssim 0$ spans on the centerline from which the sheets are shed. Figure 21 shows the entire structures from two perspectives. To clearly see the yellow $h \lesssim 0$ sheets, figure 22 lops off upper parts of the trefoil.

t=4.8 r1d015 centerline budgets Similar to how figure 16 at $t = 3.6$ marks in red the centerline spans with the strongest $\min(\epsilon_h) < 0$, for $t = 4.8$ in figure 21 marks those spans with with red hashes. Spans whose extent on both the centerline in figure 23 and the isosurfaces is indicated by: one end by the green s_g , then continues to 2/3rds of the way to a s_d mark from another $s_d - s_g$ pair.

The maroon s_f positions are no longer part of the ongoing reconnection, but are on a $h > 0$ zone that is becoming an upper vortex rings. While the red hashes and the s_d and s_g marks are becoming part of a lower ring.

The sideview in figure 21b shows this more clearly.

Further remarks:

- In figure 23a the s_d mark the primary $\min(h) < 0$ positions and in 23c the positions of $\max(\epsilon_\zeta)$, enstrophy dissipation.
- The $\epsilon_h \lesssim 0$ spans with red hashes show that the reconnection between the loops is between segments on those loops and is not simply point-to-point as with Lamb-Oseen.
- The yellow vortex sheets at $t = 4.8$ now encompass almost the entire interior within the trefoil.

L-O Comparing figure 21 to Lamb-Oseen in figure 18, the only similarity is that reconnection is forming between a primary marker and its opposing point. However the primary L-O reconnection markers are not the s_d , but the s_f^+ at local $\max(h_f)$ points. Locations with stretching, $\zeta_p > 0$, not compression. Part of the dynamics responsible for why the algebraic and Lamb-Oseen reconnection structures are so different.

- While Lamb-Oseen creates isolated braids that quickly dissipate, and shut down enstrophy production, the algebraic profiles shed vortex sheets. Sheets whose mutual interactions that can accelerate enstrophy production.

In figure 22 the upper, blue $h > 0$ zone has been lopped off to reveal the full extent and nature of the vortex sheets.

Centerline budgets and bridge formation. Up through $t = 3.6$ the centerline budget profiles have largely been used to identify the origins of the divergent evolution between the two types of initial vorticity profiles. What can the $t = 3.6$ centerline budgets tell us about the dynamics and structures during the next phase?

First question: Why is so little negative helicity ($h < 0$) seen on the centerlines? Despite the presence of neighboring $h < 0$ vortex sheets,

A likely contributing factor is the spans of strong $\epsilon_h < 0$ on the centerlines can act as sponges that remove centerline $h < 0$.

Second: What is the local dynamics when the trefoil starts to break into two rings? At $t = 3.6$, the three s_d and the opposing s_f - s_g are all locations with local $\min(h_f)$ and $\min(\zeta_p)$, indicating local compression and pinching along the vortex lines on both sides of the developing reconnection bridges. Probably due in part to the interactions between the bridges' two ends in three-dimensions.

Third: For how long does this compression/pinch persist? In $t = 4.8$ figure 23, the local $\min(h_f)$ and $\min(\zeta_p)$ diagnostics that foreshadowed reconnection for $t \leq 3.6$ still have coincident large negative spikes. However these are now located within the developing upper ring, far from the three developing reconnections. And unlike at $t = 3.6$, are not adjacent to s -spans with significant enstrophy production, $\zeta_p > 0$.

Fourth: Even as the compression/pinch dynamics subsides at $t \sim 4.8$, the enstrophy continues to grow. On the centerlines this is because the yellow, local $\min(\epsilon_h)$ s_d points still have local enstrophy production maxima, $\max(\zeta_p) > 0$. And overall is because for $t \geq 4.8$, most of the enstrophy production is coming from the growth of the $h < 0$ vortex sheets that that now envelop the lower ring and the bridges that connect the upper and lower rings.

Why is the creation of $h < 0$ sheets so important? Starting with these two reasons. First, by creating $h < 0$ zones, the vorticity in the $h > 0$ zones can grow; this breaks the early, pre-viscous, helicity conservation constraint upon vorticity growth. Second, by spreading the vorticity into sheets, the enstrophy in figure 2 can continue to grow during the first phase of reconnection; unlike the Lamb-Oseen enstrophy in figure 1. Which sets up the next stage as those sheets begin to interact with one another at $t = 6$.

t=6 The last set of r1d015 isosurfaces are for $t = 6$ in figure 24. Instead of a finding a centerline vortex, there is a higher vorticity isosurface within the low vorticity isosurface. This $t = 6$ figure represents when the first phase of reconnection ends, defined as the time t_x when the $\sqrt{\nu}Z(t)$ converge in figure 3 and the shedding of $h < 0$ sheets has ended. The views of the isosurfaces at $t = 6$ in figure 24 are similar to those at $t = 4.8$ in figures 21 and 22: (a) a side view of the entire trefoil; and (b) a plan view of the lower ring, taken from the subdomain outlined in 24a. With differences.

The side view in figure 24a shows that the legs of the lower ring have separated from the upper ring, with connecting bridges whose inner, large- ω isosurfaces are winding around one another. Such as in the upper right, with some wrapping of the helicity-mapped isosurface about the core. This has some similarities to how the Lamb-Oseen upper and lower rings in figure 19 with connecting bridges at $t = 4$. Bridges whose ends then wrap about the rings in figure 20. Except that for Lamb-Oseen the bridges transform into isolated braids in figure 20. Not broad vortex sheets.

What the experiments can visualize with Lagrangian markers are only the strongest isolated vortices. What those experiments miss are the low vorticity sheets, like those at $t \geq 4.8$ in figure 22. In this sense, the algebraic large- ω bridges in figure 24a, are a better representation of recent directly observed experimental vortices [16, 17] than Lamb-Oseen bridges, such as in figures 19 and 20.

The plan view in figure 24b shows the beginnings of the next phase, with changes in the pigmentation on the sheets of the lower ring as they start wrapping around one another. The pigmentation changes from the almost all yellow, and some red, at $t = 4.8$ in figure 22 to pigmentation at $t = 6$ in figure 24b that varies from red to yellow to green. Along the leg that runs from lower right to the upper left, there is orange ($h < 0$) coming out of the bridge in the lower right, yellow ($h \lesssim 0$) on the shed sheet in the middle, then green ($h \gtrsim 0$) on the left that is wrapping around the bridge and another sheet. This variation in color suggests that the sign for the vortical velocity $\mathbf{u} \cdot \hat{\omega}$ is also changing, which implies stretching along the legs.

Given that these stretched sheets are wrapping around the bridges and their neighboring sheets, a configuration has been created with all the elements required to invoke the Lundgren model [19] for stretched spiral vortices. This is the only analytic model that generates the growth of enstrophy required to generate a $-5/3$ Kolmogorov-like spectra. Which also implies the generation of a dissipation anomaly (1). Work on the details of the responsible inter-sheet dynamics is in progress.

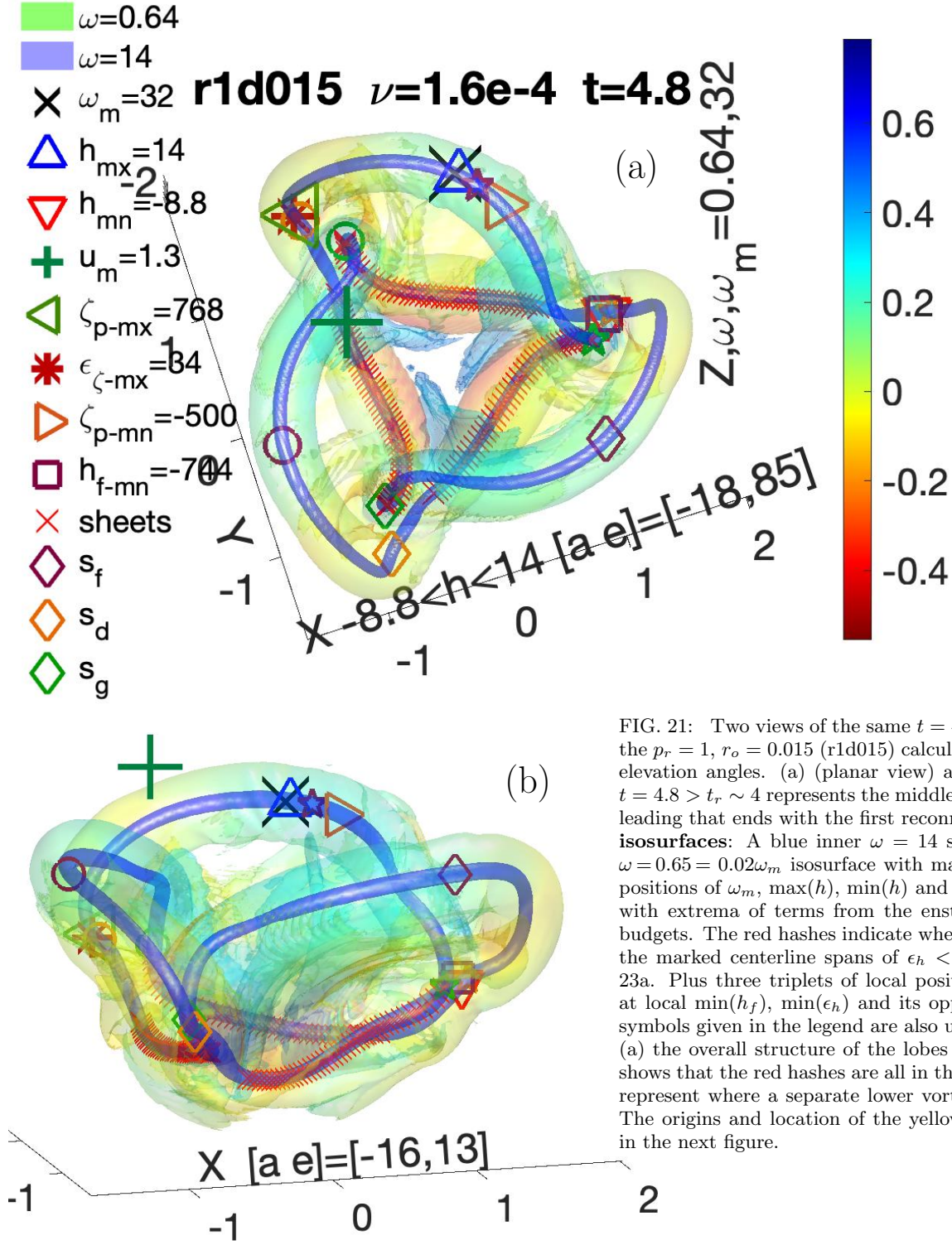


FIG. 21: Two views of the same $t = 4.8$ isosurfaces from the $p_r = 1, r_o = 0.015$ (r1d015) calculation from different elevation angles. (a) (planar view) and (b) (side view). $t = 4.8 > t_r \sim 4$ represents the middle of the initial phase leading that ends with the first reconnection at $t_x=6$. **ω -isosurfaces:** A blue inner $\omega = 14$ surface and a small $\omega = 0.65 = 0.02\omega_m$ isosurface with mapped helicity. The positions of $\omega_m, \max(h), \min(h)$ and u_m are given along with extrema of terms from the enstrophy and helicity budgets. The red hashes indicate where sheets arise from the marked centerline spans of $\epsilon_h < 0$ in budget figure 23a. Plus three triplets of local positions s_f, s_d and s_g at local $\min(h_f), \min(\epsilon_h)$ and its opposing points. The symbols given in the legend are also used in figure 23. In (a) the overall structure of the lobes is emphasized. (b) shows that the red hashes are all in the lower portion and represent where a separate lower vortex ring is forming. The origins and location of the yellow regions are given in the next figure.

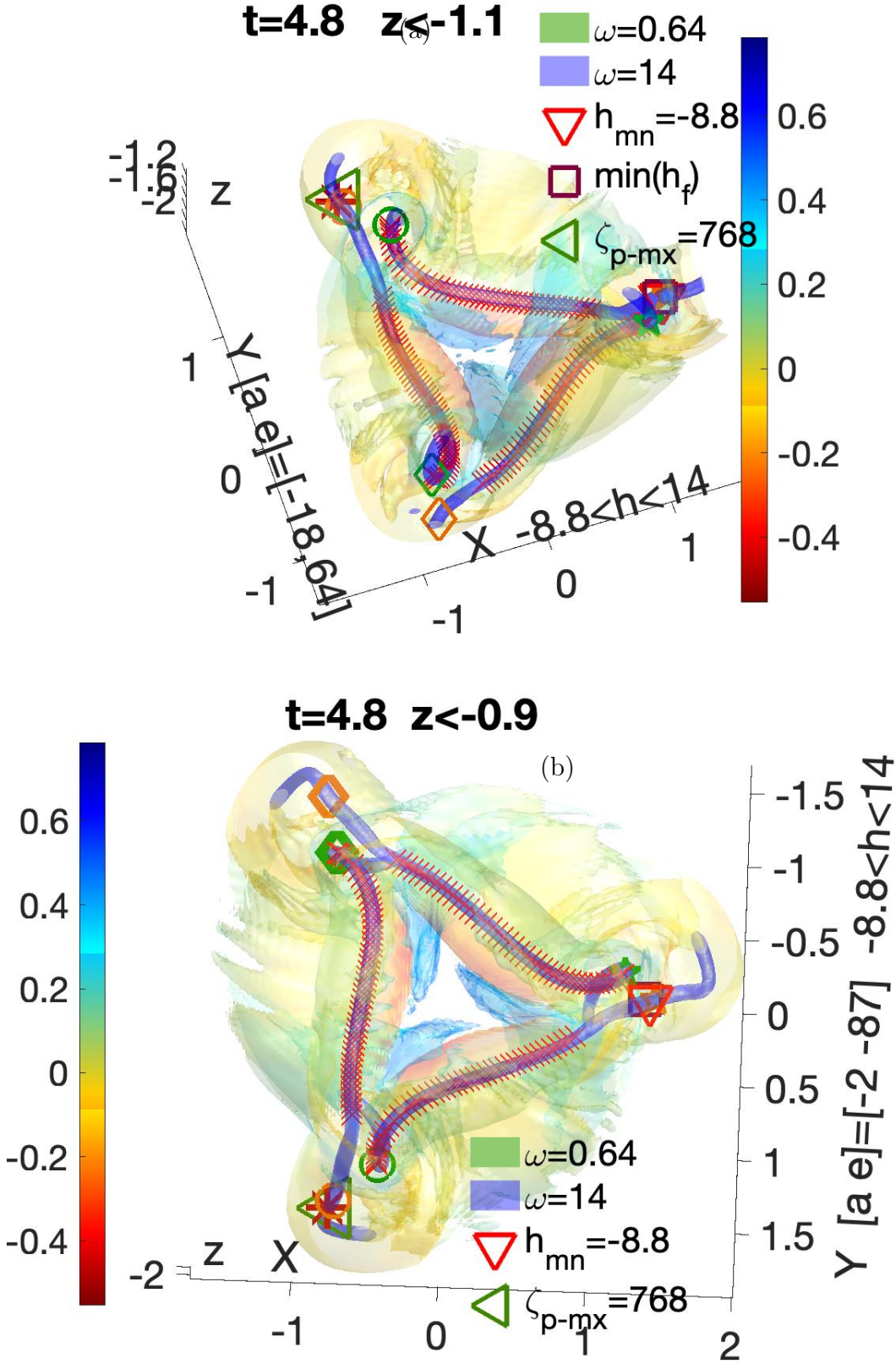


FIG. 22: Two views of the $t = 4.8$ lower region for $z < -1.1$ and -0.65 respectively, with each perspective is dominated by yellow $h \lesssim 0$: (a) looking down; (b) looking up with the domain flipped across a line from $[x \ y] = [-1 \ 1.5]$ (green triangle) to the $[x \ y] = [1 \ -1]$ corner, with some of the upper $h > 0$ zone included. It is also rotated a bit about the z -axis to give a flavor of how the legs of the lower ring are connecting with the bridge. Gray is where we are looking through both the lower yellow and upper blue. Some of the $h > 0$ zone is included to show the while the $h \lesssim 0$ sheets are being shed from the lower $h < 0$ centerline, they extend up to the upper $h > 0$ blue-marked centerline. The orange s_d and the opposing green s_g , both marked with \diamond 's, are highlighted to show how the legs might be starting to wind around each other.

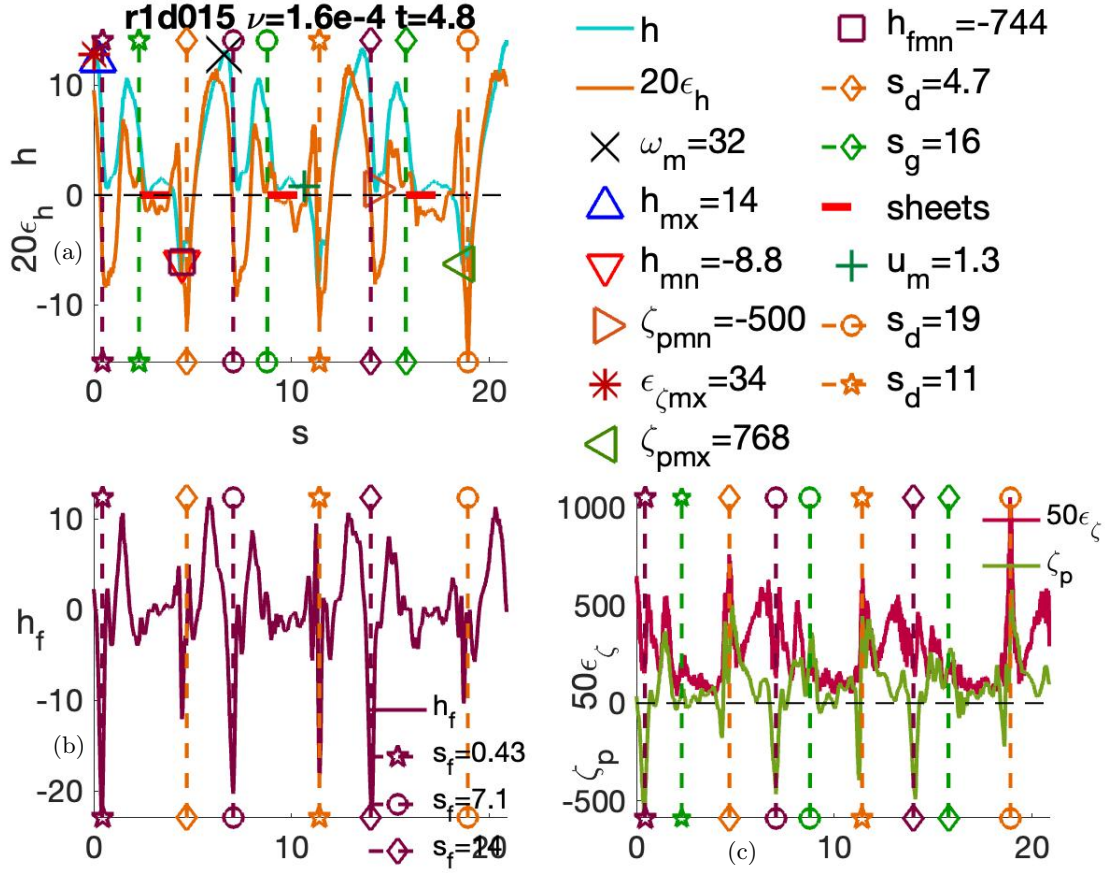


FIG. 23: Vorticity centerline profiles at $t = 4.8$ for case r1d015. Budget profiles: h , ϵ_h , h_f , ϵ_ζ and ζ_p , with added vertical dashed lines for these local positions: s_f (maroon, $\min(h_f)$), s_d (yellow, $\min(\epsilon_h)$), and s_g (green) for the s_d opposing points. The s_f are also at $\min(\zeta_p)$ and at large local enstrophy dissipation ϵ_ζ positions. The s_d are at secondary $\min(\zeta_p)$ and at local $\max(\epsilon_\zeta)$ positions. The $\epsilon_h(s) \lesssim 0$ spans over which the $h < 0$ sheets are being shed are indicated by thick, dashed red lines that are to the right of each s_g . Reconnection is forming between spans near each s_d and the red hashed patches on the opposing loops with green s_g symbols at one end. For example: the yellow diamond at $s_d = 4.7$ and the span next to the green diamond at $s_g = 16$

Algebraic $p_r=1$ $r_o = 0.015$ $t=6$.

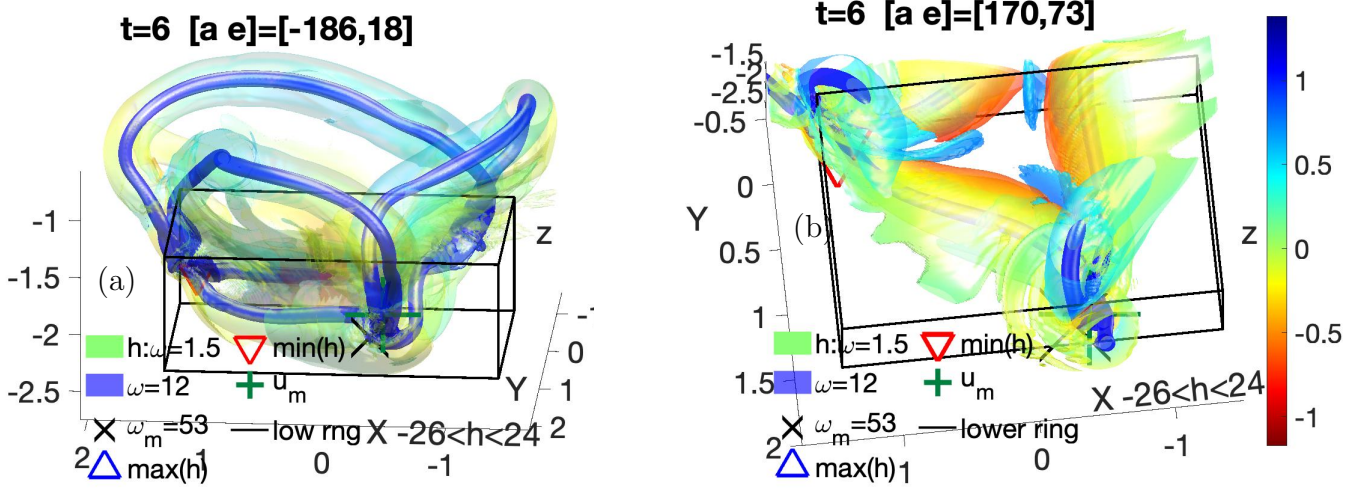


FIG. 24: Two $t = 6$ r1d015 isosurface perspectives at t_x , the end of the first reconnection, as defined by figure 3a. This is when the dissipation in figure 3b begins to accelerate, with convergence of $\epsilon = \nu Z$ at $t \approx 10$. There are two isosurfaces: inner $\omega = 12$ blue that encases the centerline; outer $\omega = 15$ with helicity-mapping. The two perspectives are similar to those at $t = 4.8$: (a) is a side view similar to that in figure 21; (b) is a cropped plan view, similar to figure 22 but with the helicity brightened. A box is drawn on both frames to show where the subdomain in (b) has been taken from the full domain in (a). In (a) the dominant structure is the pure blue $\omega = 12$ centerline isosurface with three bridges connecting the separating upper and lower vortex rings. This illustrates what direct experimental visualizations of cores are probably observing [16]. The plan view shows what those experiments cannot see: lower ω magnitude $h \lesssim 0$ vortex sheets. Two differences with figure 22 are that the sheets shed from the legs change pigmentation along their length, and they are wrapping around one another at the bridges. The ‘left’ bridge has the $\min(h)$ (red ∇) mark. The ‘right’ bridge has the ω_m (X) and u_m (green +) marks. The color change on the bottom leg is from orange $h < 0$ at the (X,+) ‘right’ bridge to green at the ‘left’ bridge. With the ‘left’ green wrapping around the ‘left’ bridge in the upper left and green from the leg on the right wrapping about ‘right’ bridge and some of the y-axis leg.

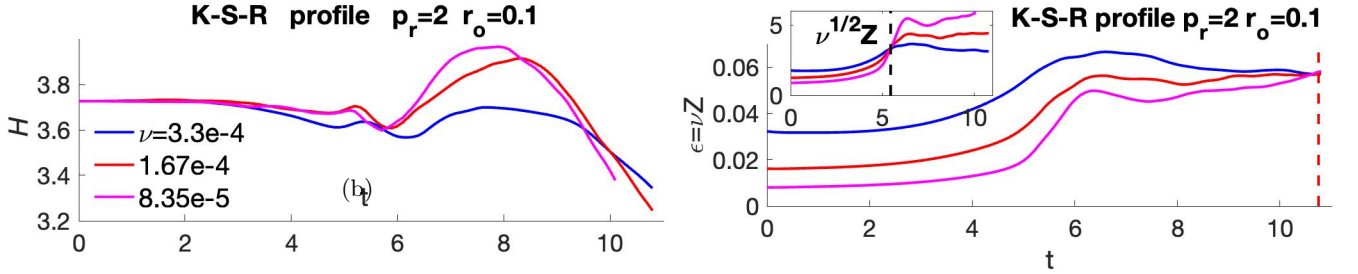


FIG. 25: For case r2d1, algebraic K-S-R profile (9) with $p_r = 2$ and $r_o = 0.1$, evolution of the dissipation rate $\epsilon(t) = \nu Z$ (a) with approximate convergence at $t_e = 10.75$, convergence of the reconnection-entrophy $\sqrt{\nu}Z(t)$ at $t_x = 5.45$ in the inset, and (b) the helicity \mathcal{H} for different viscosities. These curves are similar to those for case r1d015 in figures 2 and 3.

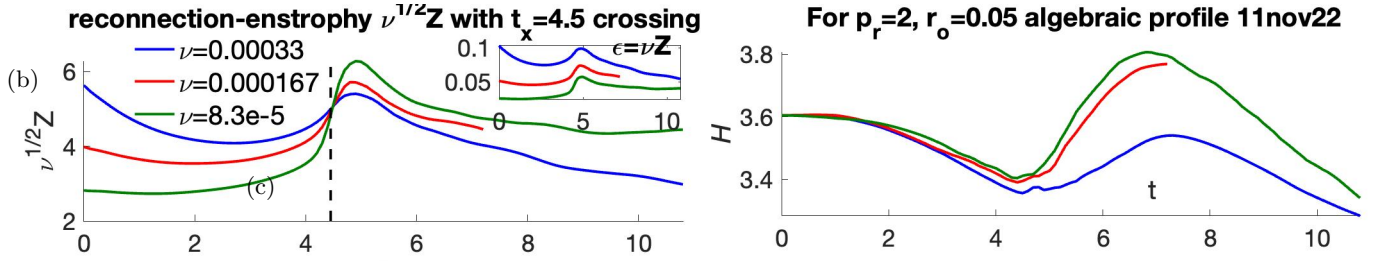


FIG. 26: For case r2d05, algebraic with $p_r = 2$ and $r_o = 0.05$, for different viscosities: (a) Convergence of $\sqrt{\nu}Z(t)$ at $t = 4.45$, (b) evolution of the dissipation rate $\epsilon(t) = \nu Z$ as an inset, and (c) the helicity \mathcal{H} . Case r1d006 ($p_r = 1$, $r_o = 0.006$) has similar $Z(t)$, $\sqrt{\nu}Z(t)$ and $\mathcal{H}(t)$ evolution and incipient vortex sheets because for both, the $(2\pi)^3$ domain is too restrictive when the core radius is very thin.

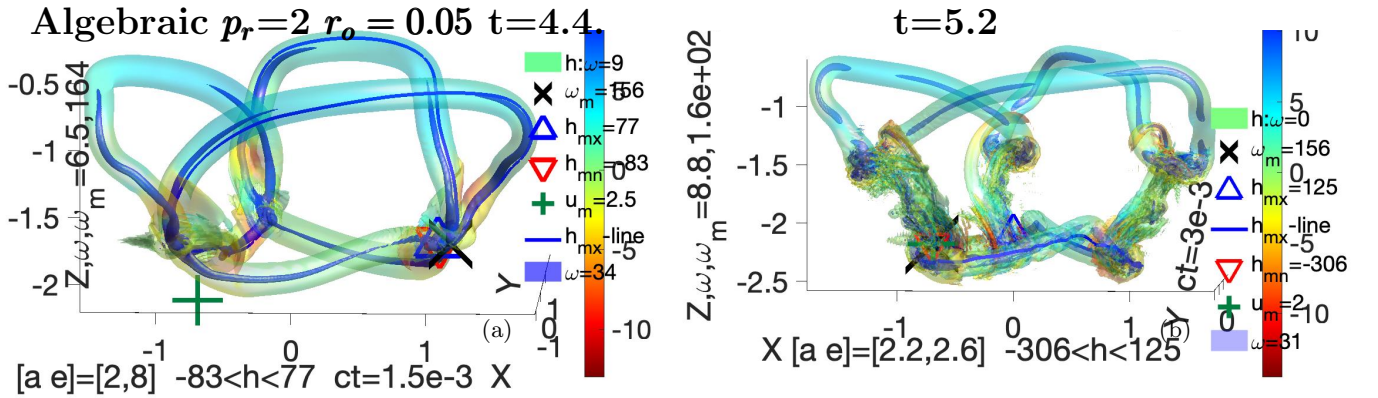


FIG. 27: For r2d05 side views at $t = 4.4$ and 5.2 . (a) At time $t = t_x = 4.4$, when the $\sqrt{\nu}Z(t)$ cross, a vortex sheet is being generated. (b) Which become connecting bridges at $t = 5.2$. High ω isosurfaces are used instead of vortex lines to indicate the centerlines.

E. Reconnection-dissipation structures for K-S-R $p_r = 2$

To finish the cases, a few results from the two K-S-R $p_r = 2$ cases r2d1 and r2d05 are included. Recall that due to stability (14), these profiles are stable unless the azimuthal wavenumber m (13) is very large. For case r2d1, the evolution of Z , $\sqrt{\nu}Z$ and \mathcal{H} mirrors that of case r1d015 in figure 2. This includes strong convergence of $\sqrt{\nu}Z$ at the same time of $t_x \simeq 6$, and approximate convergence of the dissipation rate $\epsilon = \nu Z$ at $t_\epsilon \approx 10$, with similar post-reconnection $\mathcal{H}(t)$ growth, then decay. The evolution of its three-dimensional structures is also similar.

The calculations with thinner initial algebraic cores (r2d05 and r1d006) behave differently. Both generate $\sqrt{\nu}Z$ convergence, but earlier than r2d05 and r1d015, and both fail to generation dissipation rate ϵ convergence. And for r2d05, the post-reconnection vortex structures in figure 27 have similarities with the Lamb-Oseen braids in figure 20.

These final results are likely due to the constraints imposed by the three-fold symmetry and the confined $(2\pi)^3$ periodic domain. It has previously been shown that if the core thickness is thinner [1] or the Reynolds number is higher [2], larger domains are required to get convergence of $\sqrt{\nu}Z$. And that by breaking these constraints [2], the calculation can attain the accelerated entrophy growth required for first $\sqrt{\nu}Z(t)$ convergence, then approximate convergence of the dissipation rates $\epsilon = \nu Z$ by a ν -independent time. Which is not possible for the final r2d05 and r1d006 calculations due to those constraints. Full discussion of these questions using new calculations in larger domains and a wider range of viscosities will be in a paper in preparation.

IV. SUMMARY

A. Concluding remarks.

The critical points in this paper are:

- Demonstrating that the enstrophy and helicity at reconnection depend upon the initial vorticity profile when vortex knots have the same initial trajectory and circulation.
- Vortex centerline diagnostics that demonstrate how the evolution for different initial profiles diverges.
- Explaining the structural differences that form during the first reconnection. Vortex bridges/braids for the Gaussian/Lamb-Oseen profile and vortex sheets for all the algebraic profiles.
- Not covered are the interactions between the vortex sheets of the widest algebraic profiles that lead to ν -independent convergence of ϵ and finite ΔE_ϵ (1).
That will be the topic of another paper that extends to later times the previous calculations of perturbed trefoil knots in domains that grow as the viscosity decreases [2].

Only the two outlying cases (Gd05 and r1d015) have been discussed in detail. For each, these are the critical questions:

- 1) Is it subject to infinitesimal instabilities?
- 2) How does its $t = 0$ stability influence its reconnection-time behavior?
- 3) And does that behaviour allow to finite energy dissipation to form, or not?

The answer to 1) comes from recent mathematics [15] that shows that initial profiles can be subject to instabilities when the initial state has small, but not tiny, perturbations. If so, then the mathematics of instabilities upon a columnar vortex [14], illustrated in figure 6, can be used to show that for almost all wavenumbers, there is a Richardson number dependent instability (12), as in figure 5. This develops despite the Lamb-Oseen profile being the usually successful and favorite choice of the engineering community. The resulting instability-induced proliferation of $\omega=0$ -contours is illustrated by the $t = 1.2 \omega_y$ cross-section in figure 8. A property previously observed for perturbed anti-parallel vortices [7, 9].

In contrast, the regularized $p_r = 1$ and $p_r = 2$ algebraic profiles (9) are almost always stable, with a comparison ω_y cross-section given in figure 7.

How can those small $t \gtrsim 0$ differences be the origin of the dramatic post-reconnection differences? New diagnostics are required because with the usual diagnostics of $Z(t)$ and $\mathcal{H}(t)$, there are few differences between cases until reconnection truly begins.

The most that the mapped-helicity isosurfaces can tell us about the dynamics is that around regions of negative helicity $h < 0$, sometimes just spots of yellow or red, viscous reconnection develops as the nonlinear timescale of $t_r \sim 4$ is approached. What the isosurfaces cannot explain is why the new structures that are generated are so different. Bridges and braids for Lamb-Oseen and isosurface sheets for all of the algebraic profiles. What is needed is a set of diagnostics that can follow the dynamics of the interiors before the enstrophy $Z(t)$ and the helicity $\mathcal{H}(t)$ diverge after $t \sim t_r$.

2a) The terms from the enstrophy and helicity budget equations (5,6) are another set of diagnostics that might provide evidence for the early origins for the differences between cases. These could be mapped onto isosurfaces, as done for the helicity, or on the centerlines. When mapped onto the isosurfaces, their variations are too weak to be useful. In contrast, when mapped onto the centerline vortices (17), the variations are substantial.

2b) The chosen centerline diagnostics in this paper are h , ϵ_h , $|\omega| = \sqrt{\zeta}$, h_f , ϵ_ζ and ζ_p , and are arranged into four panels. Plus vertical dashed lines in every panel at positions related to local extrema. This includes the positions of local $\min(h_f)$, local $\min(\epsilon_h)$ and their nearest positions on the opposite loop of the trefoil. By following and comparing their extrema between the panels and the isosurfaces, a picture of the evolution emerges.

The diagnostics that carry the most information at early times are the centerline positions of local $\min(h_f)$, h -flux minima (6). At the earliest times shown, $t = 1.2$ for r1d015 algebraic profile and $t = 0.4$ for Lamb-Oseen case Gd05, the local $\min(h_f)$ can be matched with several extrema. Local minima and maxima of the helicity dissipation ϵ_h and minima of the enstrophy production ζ_p (5), as given in figures 9 and 10. For algebraic case r1d015, from $t = 1.2$ to when reconnection begins, the relative centerline positions of these extrema are stable. Allowing the $h < 0$ zones on the new lower ring to gradually shed $h < 0$ vortex sheets.

In the period $t = 1.2$ to 2.4 , the relative positions on the Lamb-Oseen centerline profiles are not stable. Figure 11 at $t = 1.2$ has six roughly equivalent positive and negative excursions of ϵ_h around positions of local compression, local $\min(\zeta_p) < 0$. Likely due to local interactions with the instability-induced, oppositely-signed patches shown in figure 8. Three are associated with the s_f points. The other three with their s_o opposing points.

The Lamb-Oseen s_f points return to something akin to normal for the budget curves at $t = 2.4$ in figure 12. However, the damage has been done and when reconnection begins at $t = 3.6$, the reconnection structures form only between the $t = 1.2$ extrema points.

3) It is these differences in the respective $t \leq 2.4$ budgets that determine whether the post-reconnection structures are braids or sheets. And whether finite energy dissipation can form. Post-reconnection Lamb-Oseen first generates bridges, as at $t = 4$ in figure 19. Then progresses to braids at $t = 4.4$ in figure 19. With only a sort-lived growth in the enstrophy $Z(t)$ and energy dissipation $\epsilon(t)$ in figure 1 before Z and ϵ decay.

This contrasts with the algebraic profiles that do not have this instability, or any excessive local compression. And due to this, the helicity transport h_f is able to spread $h < 0$ along the centerline. From which $h < 0$ vortex sheets can be shed as the trefoil self-reconnects, as shown in figure 16a,c at $t = 3.6$ and figures 21 and 22 at $t = 4.8$. Figure 24 at $t = 6$ shows how those sheets, when interacting, can allow the enstrophy growth to accelerate and convergent energy dissipation rates ϵ to be achieved. Leading to evidence for a dissipation anomaly with finite ΔE_ϵ (1). With the only evidence for bridges or braids from the algebraic calculation coming from internal higher- ω isosurfaces, as in figure 24.

B. Discussion

The centerline budget diagnostics introduced here will next be applied to extensions, or variations upon, two existing calculations. First, extensions of the earlier, perturbed trefoils in very large domains [2] to higher Reynolds numbers and later times. Second, versions of recent calculations of interacting orthogonal vortices [18]. For both, approximately convergent ν -independent dissipation rates $\epsilon = \nu Z$ develop after the interacting vortices flatten, ν -independent convergent $\sqrt{\nu}Z$ is observed at t_x and the sheets wrap around one another.

On the orthogonal isosurfaces, the mapped helicity indicates that within that wrapping, the vortex stretching is vortical. Observations that are consistent with the Lundgren spiral vortex model [19] for generating a $-5/3$ energy spectrum. At the time (circa 1982), a mechanism for creating wrapped and stretched vortex sheets within a turbulent flow had not been demonstrated. Although in retrospect, this is probably what stills [20] taken from the earliest color, three-dimensional animations of interacting vortices are showing.

The recent orthogonal vortices [18] were initialized with a Lamb-Oseen profile, and did not develop $t \gtrsim 0$ negatively-signed ghost vortices. Probably because those vortex tubes were not curved, but straight, so were not modified by the solenoidal projection as in initialization step 4 in section II A. Meaning, they lacked a perturbation on their outer edge similar to that in figure 5. With the only perturbations being inherently numerical and tiny. The additional analysis [15] given after stating the stability function $J(\rho)$ (12) for columnar vortices [14] says that tiny perturbations should not generate strong instabilities. That is, if a Lamb-Oseen profile is applied to straight vortex tubes, there will not be any instabilities capable of generating negatively-signed ghosts like those in figure 8 and earlier work [9].

Other Lamb-Oseen calculations. In the recent review [21] of the state of numerical vortex reconnection, a reconnection-to-bridges to braids cascade paradigm was presented based upon the results from Lamb-Oseen profile calculations, without any examples given of a second step in that cascade. Given the contrasting enstrophy evolution of the algebraic calculations, how should that paradigm be changed?

The changes are substantial, with the algebraic alternative being a two-step process instead of a cascade. First the period that ends at t_x with $\sqrt{\nu}Z(t)$ convergence, generation of $h < 0$ vortex sheets and completion of the first reconnection. Next the period $t_x < t \lesssim t_\epsilon \approx 2t_x$ during which the sheets wrap around one another, leading to convergent $\epsilon = \nu Z$. As that large ϵ persists, finite-time, finite ΔE_ϵ (1) forms.

Furthermore, because that review [21] focuses upon their recent trefoil calculation [3] as the latest support for the reconnection-to-braids paradigm, it is fair to ask whether the instabilities identified here extend to all the cited Gaussian/Lamb-Oseen calculations in that review.

They probably do, going back to the first in 1989 [22]. The effects of such instabilities were first clearly identified for an Euler calculation using an elongated Gaussian profile [7] and were then clarified by 2013 anti-parallel analysis [9] that shows $t \sim 0$ $\omega = 0$ contours that are more intense than those in figure 8. If the authors of that recent review [21] disagree with the analysis behind that conclusion, what would be useful would be a submission to Physical Review Fluids that applied the centerline diagnostics introduced here to another one of their recent calculations.

Acknowledgements

I would like to thank the Isaac Newton Institute for Mathematical Sciences for support and hospitality during the programme *Mathematical Aspects of Fluid Turbulence: where do we stand?* in 2022, when work on this paper was undertaken and supported by grant number EP/R014604/1. Including interactions with, among others, A. Leonard and M. Musso. I thank E. Brambley at Warwick for clarifying crucial elements during the final preparation. Computing resources have been provided by the Scientific Computing Research Technology Platform at the University of Warwick.

-
- [1] R.M. Kerr, Trefoil knot timescales for reconnection and helicity, *Fluid Dynamics Res.* **50**, 011422 (2018).
 - [2] R.M. Kerr, Enstrophy and circulation scaling for Navier-Stokes reconnection, *J. Fluid Mech.* **839**, R2 (2018).
 - [3] H. J. Yao, Y. Yang and F. Hussain Dynamics of a Trefoil Knotted Vortex, *J. Fluid Mech* **923**, A19 (2021).
 - [4] X. Zhao and C. Scalò, Helicity Dynamics in Reconnection Events of Topologically Complex Vortex Flows, *J. Fluid Mech.* , (2021).
 - [5] A. Alexakis and L. Biferale, Cascades and transitions in turbulent flows, *Physics Reports* , 767 (2018).
 - [6] L. Rosenhead, The Formation of Vortices from a Surface of Discontinuity, *Proc. Roy. Soc. A* **134**, 170 (1931).
 - [7] MD Bustamante and RM Kerr, 3D Euler about a 2D symmetry plane, *Physica D* **237**, 1912 (2008).
 - [8] R.M. Kerr, Swirling, turbulent vortex rings formed from a chain reaction of reconnection events, *Phys. Fluids* **25**, 065101 (2013b).
 - [9] R.M. Kerr, Fully developed hydrodynamic turbulence from a chain reaction of reconnection events, *Procedia IUTAM* **9**, 57 (2013a).
 - [10] R.M. Kerr, Bounds for Euler from vorticity moments and line divergence, *J. Fluid Mech.* **729**, R2 (2013b).
 - [11] H.K. Moffatt, Helicity and singular structures in fluid dynamics, *Proc. Nat. Acad. Sci.* **111**, 3663 (2014).
 - [12] R.M. Kerr, Topology of interacting coiled vortex rings, *J. Fluid Mech.* **854**, R2 (2018).
 - [13] S. Xiong and Y. Yang, *Phys. Fluids* **31**, 4 (2019). Construction of knotted vortex tubes with the writhe-dependent helicity
 - [14] L.N. Howard and A.S. Gupta, On the hydrodynamic and hydromagnetic stability of swirling flows, *J. Fluid Mech.* **14**, 463 (1961).
 - [15] T. Gallay and D. Smets, Spectral stability of inviscid columnar vortices, *Anal. PDE* **13**, 1777 (2020).
 - [16] D. Kleckner and W.T.M Irvine, Creation and dynamics of knotted vortices *Nature Phys.* **9**, 253 (2013).
 - [17] M. W. Scheeler, D. Kleckner, D. Proment, G. L. Kindlmann and W.T.M. Irvine Helicity conservation by flow across scales in reconnecting vortex links and knots, *Proc. Nat. Acad. Sci.* **111**, 15350 (2014).
 - [18] R. Ostillo-Mónico, R. McKeown, M.P. Brenner, S. M. Rubenstein and A. Pumir, Cascades and reconnection in interacting vortex filaments, *Phy. Rev. Fluids* **6**, 074701 (2021).
 - [19] T. S. Lundgren, Strained spiral vortex model for turbulent fine structure, *Phys. Fluids* **25**, 2193 (1982).
 - [20] R. M. Kerr, Higher order derivative correlations and the alignment of small-scale structures in isotropic numerical turbulence, *J. Fluid Mech.* **153**, 31 (1985).
 - [21] J. Yao and F. Hussain, Vortex Reconnection and Turbulence Cascade, *Annu. Rev. Fluid Mech.* **54**, 317 (2022).
 - [22] M.V. Melander and F. Hussain, Cross-linking of two antiparallel vortex tubes, *Phys. Fluids A* **1**, 633 (1989).
 - [23] R. M. Kerr, Evidence for a singularity of the three-dimensional, incompressible Euler equations, *Phys. Fluids A* **5**, 1725 (93a).
 - [24] L.F. Richardson, *Weather Prediction by Numerical Process*. Cambridge University Press. (1922).
 - [25] J. Tribbia, 2020 Normal Mode Functions and Initialization., In *Modal View of Atmospheric Variability* (ed. N. Zagar and J. Tribbia), pp. 63–78. Springer.
 - [26] D. Virk, F. Hussain and R.M. Kerr Compressible vortex reconnection, *J. Fluid Mech.* **304**, 47 (1995).
 - [27] R.M. Kerr and F. Hussain, Simulation of vortex reconnection, *Physica D* **37**, 474 (1989).

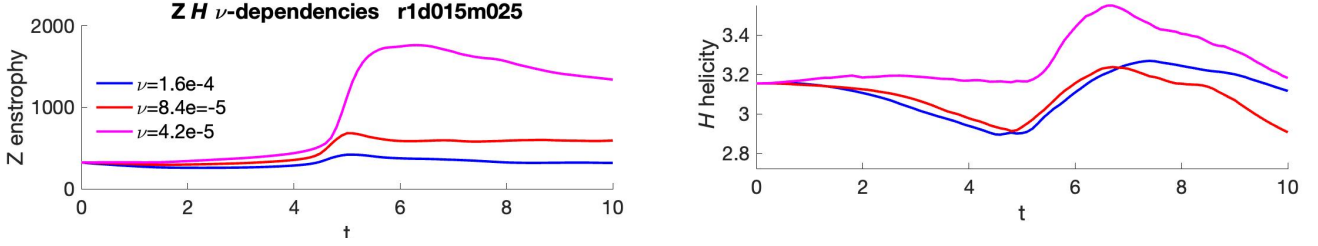


FIG. 28: Cut-off Rosenhead time evolution. Left: Enstrophy Right: Helicity. Like algebraic in figure 2 the enstrophy grows as opposing segments are interacting for $t_r = 4 < t < 6$. However after that, like Lamb-Oseen in figure 1, $Z(t)$ then decays. And there is more persistent growth of $\mathcal{H}(t)$ like Lamb-Oseen.

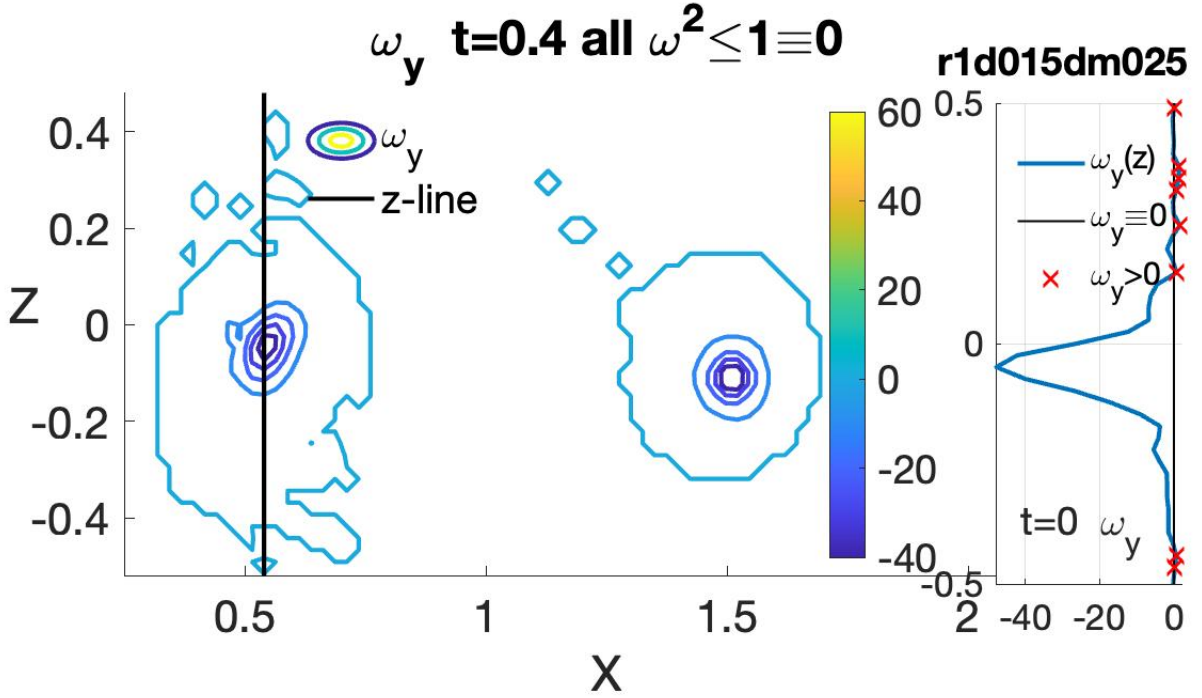


FIG. 29: Cut-off ω_y Rosenhead $x-z$. Left: $t = 0.4$ cross-section with vertical line through $\min(\omega_y)$. Note several contours of $\omega_y \equiv 0$. Right: Profile of ω_y through $t = 0$ line through $\min(\omega_y)$. Note several positions in red where there oppositely signed ($\omega_y > 0$) spots. Similar to what is found for Lamb-Oseen in figure 4.

Appendix A: Results for cut-off Rosenhead profiles.

In this appendix the evolution of an algebraic profile with a severe cut-off at $\rho_+ = 0.025$. The objective is to demonstrate that steep cut-offs can be as much of a problem as the chosen profile. The minimum resources were expended and detailed analysis (3D graphics) is not provided. This case behaves in many ways more like the Lamb-Oseen profile than the other algebraic profiles. There is growth of the enstrophy $Z(t)$ over $t_r = 4 < t < 6$ as in algebraic in figure 2. But growth of $Z(t)$ is then suppressed as $\mathcal{H}(t)$ grows, more like Lamb-Oseen in figure 1.

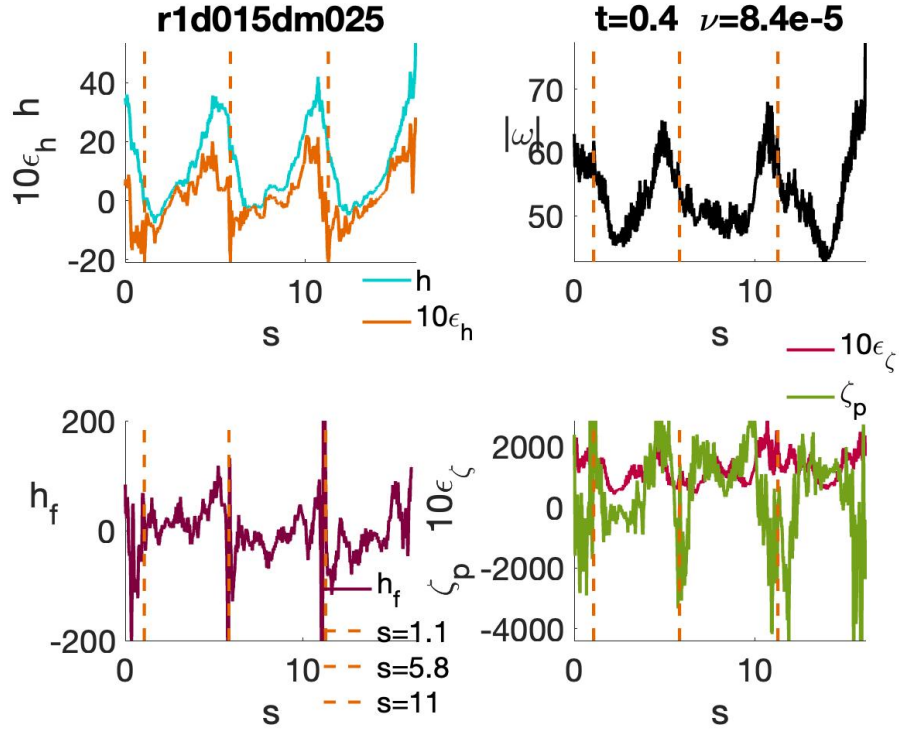


FIG. 30: Cut-off ω_y Rosenhead $x-z$ at $t = 0.4$ vorticity centerline profiles of h , h_d , $|\omega|$, h_f , ϵ_Z and Z_p . In most respects this is like early times for both the Lamb-Oseen and algebraic cases, Lamb-Oseen at $t = 0.4$ and untruncated algebraic at $t = 1.2$ in figures 10 and 9 respectively. There are three positions of significance. Chosen by local negative helicity dissipation $\min(\epsilon_h)$ but also at or near local $\min(h_f)$ of the helicity flux and local compression $\min(\zeta_p)$.

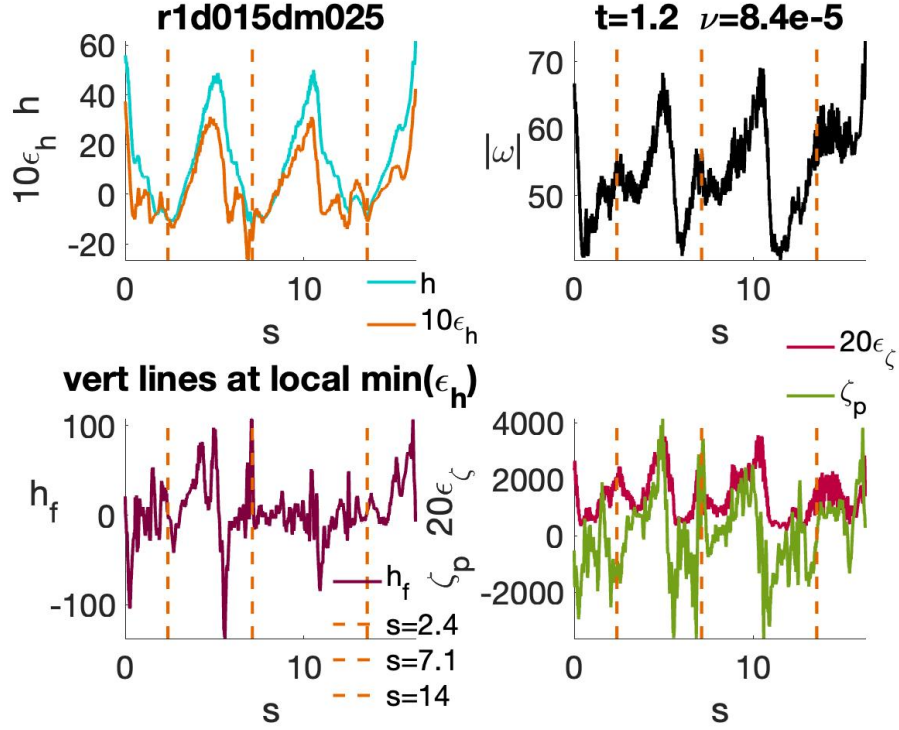


FIG. 31: Cut-off ω_y Rosenhead $x-z$ Vorticity centerline profiles at $t = 1.2$. This is unlike the regular centerline profiles at $t = 0.4$ just given and unlike the untruncated algebraic at $t = 1.2$ in figure 9, the relationships between the local $\min(u_d)$ positions and the other properties are muddled. However, it is not as extreme as the Lamb-Oseen six-fold symmetry in figure 11.